



Review

# High-Performance Photodetectors Based on Nanostructured Perovskites

Chunlong Li <sup>1,\*</sup>, Jie Li <sup>2</sup>, Zhengping Li <sup>1</sup>, Huayong Zhang <sup>1</sup>, Yangyang Dang <sup>3,4,\*</sup> and Fangong Kong <sup>1,\*</sup>

- <sup>1</sup> Key Laboratory of Pulp and Paper Science & Technology of Ministry of Education, Qilu University of Technology, Shandong Academy of Sciences, Jinan 250353, China; knje@163.com (Z.L.); headingzhy@126.com (H.Z.)
- <sup>2</sup> International College of Optoelectronic Engineering, Qilu University of Technology, Shandong Academy of Sciences, Jinan 250014, China; jiejie19831228@163.com
- <sup>3</sup> Shandong Provincial Key Laboratory of Laser Polarization and Information Technology, School of Physics and Physical Engineering, Qufu Normal University, Qufu 273100, China
- <sup>4</sup> Tianjin Key Laboratory of Molecular Optoelectronic Sciences, Department of Chemistry, School of Sciences, Collaborative Innovation Center of Chemical Science and Engineering, Tianjin University, Tianjin 300072, China
- \* Correspondence: 15650025069@163.com (C.L.); yeung\_dang@tju.edu.cn (Y.D.); kfgwsj1566@163.com (F.K.)

**Abstract:** In recent years, high-performance photodetectors have attracted wide attention because of their important applications including imaging, spectroscopy, fiber-optic communications, remote control, chemical/biological sensing and so on. Nanostructured perovskites are extremely suitable for detective applications with their long carrier lifetime, high carrier mobility, facile synthesis, and beneficial to device miniaturization. Because the structure of the device and the dimension of nanostructured perovskite have a profound impact on the performance of photodetector, we divide nanostructured perovskite into 2D, 1D, and 0D, and review their applications in photodetector (including photoconductor, phototransistor, and photodiode), respectively. The devices exhibit high performance with high photoresponsivity, large external quantum efficiency (EQE), large gain, high detectivity, and fast response time. The intriguing properties suggest that nanostructured perovskites have a great potential in photodetection.

**Keywords:** nanostructured perovskites; high-performance photodetector; different dimensions



**Citation:** Li, C.; Li, J.; Li, Z.; Zhang, H.; Dang, Y.; Kong, F. High-Performance Photodetectors Based on Nanostructured Perovskites. *Nanomaterials* **2021**, *11*, 1038. <https://doi.org/10.3390/nano11041038>

Academic Editor:  
Antonio Bartolomeo

Received: 18 March 2021  
Accepted: 9 April 2021  
Published: 19 April 2021

**Publisher's Note:** MDPI stays neutral with regard to jurisdictional claims in published maps and institutional affiliations.



**Copyright:** © 2021 by the authors. Licensee MDPI, Basel, Switzerland. This article is an open access article distributed under the terms and conditions of the Creative Commons Attribution (CC BY) license (<https://creativecommons.org/licenses/by/4.0/>).

## 1. Introduction

Photodetectors—the vital components of modern imaging and communication systems—have been playing an increasingly important role in modern industrial production, basic scientific research, space development, ocean exploration, military and national defense, environmental protection, medical diagnosis, transportation, and other fields. For example, ultraviolet photodetectors can be used in ozone sensing, flame sensing, etc. [1–3]. The visible photodetectors can be used in biological sensing, video imaging, and convert communications [4–7]. Infrared photodetectors can be used as infrared night vision. [8–10] The THz photodetectors can be used in the security detection of customs, airports, and other special occasions [11–13]. Therefore, the further research of photodetectors is of great significance. A semiconductor, which is essential for a photodetector, can absorb the incident photons and generate electron and hole pairs. In the presence of a built-in or applied electric field, electric current is generated when the electrodes extracted and collected photogenerated carriers. In order to obtain a high-performance photodetector with high sensitivity and fast response, the semiconductor needs to have effective charge collection, low trap state density, and high carrier mobility. Till now, a large variety of semiconductor materials have been used for constructing photodetectors, including Si [14–16], carbon nanotubes [17,18], group II–VI and III–V compounds [19–21], and remarkable progress has been made in improving the detection performance. Epitaxial growth technology

with stringent conditions, which is the most commonly used for synthesis, hampers their commercial application [22]. Therefore, it is of great significance to exploit candidates to reduce production cost and improve photodetector performance.

Recently, perovskites with a typical formula of  $ABX_3$  has attracted wide research interest in the photodetector field [23–25]. For  $ABX_3$ , A is a monovalent cation ( $CH_3NH_3^+$  (MA),  $Cs^+$ , etc.), B is the divalent metal cation ( $Pb^{2+}$ ,  $Sn^{2+}$ , etc.), and X is a halide ion ( $Br^-$ ,  $Cl^-$  and  $I^-$ ). Many properties of perovskite make it an ideal material for photodetectors. For example, ambipolar transport, low density of defects and traps within bandgap can effectively reduce the charge recombination, and thus improve the performance of photodetectors. [26] The absorption spectra can cover the UV–Visible–Infrared region by facile halide substitution, which is desirable for broadband photodetector applications [27,28]. High absorption coefficient and direct bandgap result in a fast photoresponse in a very thin perovskite layer because of short transmission distance of photogenerated carriers [29,30]. In addition, low cost and easy preparation remove obstacles in future mass preparation. For example,  $MAPbI_3$  film-based photodetectors with a metal–semiconductor–metal (MSM) structure exhibited a broad photoresponse range from 310 nm to 780 nm, with a photoresponsivity of  $3.49 \text{ A W}^{-1}$  and external quantum efficiency (EQE) of  $1.19 \times 10^3\%$  [31]. However, there is an inherent paradox to simultaneously possess both low dark currents and high photocurrents. The former requires a large number of defects or barriers that appear in polycrystalline film to inhibit the transmission of thermally excited carriers [32–34], while the latter requires single crystals with good crystallinity for effective charge transfer [35–37]. Compared with photodetectors based on polycrystalline film and bulk crystals, nanostructured photodetectors exhibit superior performances. The large surface-to-volume ratios of nanostructures result in longer photocarrier lifetime, which is conducive to higher sensitivity and responsivity. In addition, the reduced dimension shortens the carrier transmission time and improves the response speed [19,38–41]. Therefore, the performance of photodetector based on nanostructured perovskites will be better. For example, a high responsivity of  $1294 \text{ A W}^{-1}$  with a ultrahigh detectivity of  $2.6 \times 10^{14}$  Jones was obtained in  $\alpha$ - $CsPbI_3$  nanowire-based photodetector [42]. In addition, an ultrahigh response speed (19/25  $\mu\text{s}$ ) was obtained in a photodetector based on atom-thin 2D  $CsPbBr_3$  nanosheets [43]. An ultrahigh EQE over  $10^7\%$  was demonstrated by a phototransistor based on  $CsPbI_{3-x}Br_x$  quantum dots (QDs)/monolayer  $MoS_2$  heterostructure [44]. All these are enough to show that the photodetectors based on nanostructured perovskites have more advantages in ultrahigh responsivity and ultrafast response speed. There have been some reviews on nanostructured perovskite-based photodetectors. Gu et al. [45] focus on the effect of elemental composition and dimensionality of the perovskite materials on photodetector performance. Wang et al. [46] systematically summarized the synthesis, optoelectronic properties, and performance of photodetectors based on low-dimensional perovskites. Here, more emphasis is placed on the effect of the device structure and the dimension of nanostructured perovskites on the device performance.

The key parameters of photodetectors are shown in Table 1.

In this study, we will review research results in nanostructured perovskite-based photodetectors, focusing on the photodetection performance and potential mechanism. It is well known that the electrons of nanostructured perovskite are quantum confined in three directions for 0D QDs, two directions for 1D nanowires (NWs), and one direction for 2D nanosheets [45]. The band structures of the nanostructured perovskite could be heavily influenced by the quantum size effect induced by dimensionality constraint, and thus deeply affect the optoelectronic properties. Therefore, we discussed the performance of perovskite photodetectors based on 1D, 2D, and other nanostructured perovskites, respectively. Finally, a brief summary and outlook will be given to enhance the performance of the perovskite-based photodetectors.

**Table 1.** The key parameters of photodetectors.

Parameters	Definition
Photoresponsivity (R)	the ratio of the photocurrent to the incident power on the active area: $R = (I_p - I_d)/(PA)$ , where $I_p$ is the photocurrent, $I_d$ is the dark current, $P$ is the light intensity, $A$ is the active area
EQE	Photoelectric conversion efficiency. $EQE = Rhc/e$ , where $h$ is the Planck's constant, $c$ is the light velocity, $e$ is the electronic charge.
Gain (G)	The number of charge carriers through external circuit for per incident photon: $G = \tau_l/\tau_t = \tau_l(\mu V)/d^2$ , where $\tau_l$ is the carrier lifetime, $\tau_t$ is the carrier transit time, $\mu$ is the carrier mobility, $V$ is bias voltage, $d$ is the channel length
Detectivity ( $D^*$ )	$D^* = (A\Delta f)^{1/2}/NEP$ , where $A$ is the active area of the detector, $\Delta f$ is the electrical bandwidth, $NEP$ is the noise equivalent power.
LDR	LDR usually stands for "Linear Dynamic Range", defined as the range in which the current response of the photodetector is linearly proportional to the light intensity. $LDR = 20 \log (I_p^*/I_d)$ , Where $I_d$ is the dark current.
Response speed (rise/decay time)	The ability of devices to track the incident light signal.

## 2. Photodetectors

Perovskite-based photodetector devices can be divided into two categories, photovoltaic and photoconductive photodetectors. According to the spatial layout of the photoactive medium and electrodes, perovskite-based photodetector devices can be further divided into vertical type and lateral type. In general, vertical photodetectors provide fast response and low driving voltage because of the small electrode spacing with a short carrier transit length; in contrast, lateral photodetectors show slow response and high driving voltage due to their large electrode spacing. For photovoltaic photodetector, or photodiode (Figure 1a), the device structure is similar to that of solar cell configuration. Photodiodes based on perovskite polycrystalline films or single crystals are widely reported, but those based on nanostructured perovskites are rarely reported. Photodiodes typically rely on PN junction, which can provide a built-in electrical field at the junction interface to aid the electrons and holes to transport in opposite directions toward electrodes. Owing to the junction barrier at the interface, photodiodes exhibit low dark current and large detectivity. However, they suffer from low responsivity and external quantum efficiency ( $EQE \leq 100\%$ ). As for photoconductive photodetector, it can be further divided into photoconductor (Figure 1b) and phototransistor (Figure 1c). Compared with photovoltaic photodetector, photoconductive photodetector exhibits high responsivity, EQE (beyond 100%) and large gain. External voltage leading to multiple electrical carriers recycling per single incident photon should be responsible for the large gain [47–50]. However, large gain, in turn, usually results in a slow response speed because both the response time and the gain are determined by the carrier lifetime. Therefore, the intrinsic contradictions between the responsivity and response speed always exist. One solution is to fabricate phototransistor by adding gate electrode (Si) and dielectric layer ( $SiO_2$ ) to the photoconductor. The charge transport can be controlled by applying a gate voltage. It is demonstrated that phototransistor can simultaneously enhance the photoresponsivity and exhibit an ultrafast photoresponse speed [51].

### 2.1. Photoconductor

#### 2.1.1. Photoconductor Based on 2D Perovskites

Among the various perovskite compositions,  $CsPbX_3$  and  $CH_3NH_3PbX_3$  ( $MAPbX_3$ ) ( $X = Br, I$ ) have attracted more attention in photodetection. Song et al. report [43] for the first time, the preparation of atom-thin 2D  $CsPbBr_3$  nanosheets and their high-performance in flexible photodetector with solution treatment. The UV-vis absorption spectrum (Figure 2a) of the  $CsPbBr_3$  nanosheets exhibited a favorable absorption capability and a direct bandgap of about 2.32 eV. The schematic of a flexible photodetector device based on the as-fabricated

CsPbBr<sub>3</sub> nanosheet is shown in Figure 2b. The flexible photodetector exhibited a high on/off ratio ( $>10^3$ , Figure 2c), which indicated a good light-switching behavior, high responsivity of  $0.25 \text{ A W}^{-1}$  (Figure 2d) and peak EQE value of 53% (Figure 2e). The high switching ratio as shown in Figure 2f results from large absorption coefficient of the perovskites. The rise and decay times were 19 and 25  $\mu\text{s}$  (Figure 2g), respectively, which are much shorter than the previously reported [52]. The high response speed can be attributed to the high carrier transport speed caused by high crystal quality and atomic 2D plane of the CsPbBr<sub>3</sub> nanosheets. A fluctuation that was  $<3\%$  after bending for 10,000 times indicates high flexibility (Figure 2h). In addition, a fluctuation of less than 2.6% after 12 h of exposure indicates excellent stability (Figure 2i). These results show that there is a great potential for CsPbBr<sub>3</sub> nanosheets in high-sensitivity detectors.

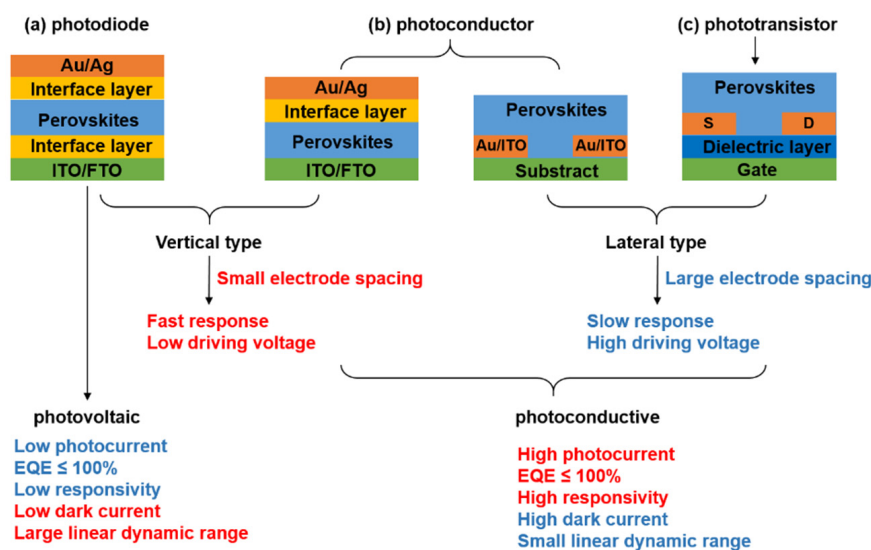


**Figure 1.** Schematic and characteristics of perovskite-based photodetectors. (a) photodiode, (b) photoconductor, and (c) phototransistor.

Qin et al. [53] successfully prepared high-quality MAPbI<sub>3</sub> with the morphologies of nanowires (NWs) and nanoplates by a simple solution immersing method. Schematic diagrams of photodetectors based on nanowire and nanoplate are shown in Figure 3a,b. The stability was tested by dozens of cycles under different illumination (Figure 3c,d). Both the photocurrent and switching ratio were maintained well, and the switching ratio was well controlled by adjusting the applied illumination intensity. The on/off ratio of the nanowire-based MAPbI<sub>3</sub> photodetector reached 314, while the on/off ratio of nanoplate-based photodetector up to 1210, which was several orders of magnitude higher than that of polycrystalline film photodetector [54]. The nanoplate-based devices usually exhibit a relatively better performance than nanowire-based devices due to the higher crystal quality with smoother surface and more regular shapes. It suggested that higher performance could be expected by further improving the crystal quality.

Due to low responsivity induced by poor charge transport of perovskites, many studies have combined perovskites with high mobility materials to increase responsivity. For example, Li et al. [55] constructed a photodetector based on CsPbBr<sub>3</sub> nanosheet/carbon nanotubes (CNTs) heterojunction to improve performance. CNTs act as a transport layer with high carrier mobility, and CsPbBr<sub>3</sub> nanosheets act as a photo absorber with strong absorption. The schematic diagram of the photodetector was illustrated in Figure 4a. The experiment proved that CsPbBr<sub>3</sub> nanosheet/CNT (6%) composite-based photoconductor exhibits almost the best responsivity. The highest external quantum efficiency (EQE) reaches 7488% (Figure 4b) and the highest responsivity reaches  $31.1 \text{ A W}^{-1}$  (Figure 4c). The on/off ratio reaches 823 (Figure 4d). A nonlinear I–V curve demonstrates Schottky contact between CsPbBr<sub>3</sub> nanosheet/CNT and electrodes. Figure 4e shows a broad LDR of

the device. The  $I-t$  curves exhibit excellent reproducibility and stability (Figure 4f). The rise and decay times were 16  $\mu\text{s}$  and 0.38 ms, respectively (Figure 4g). The high response speed indicates the rapid separation and efficient extraction of photogenerated carriers, which can be attributed to the improved electrical conductivity of CNTs.

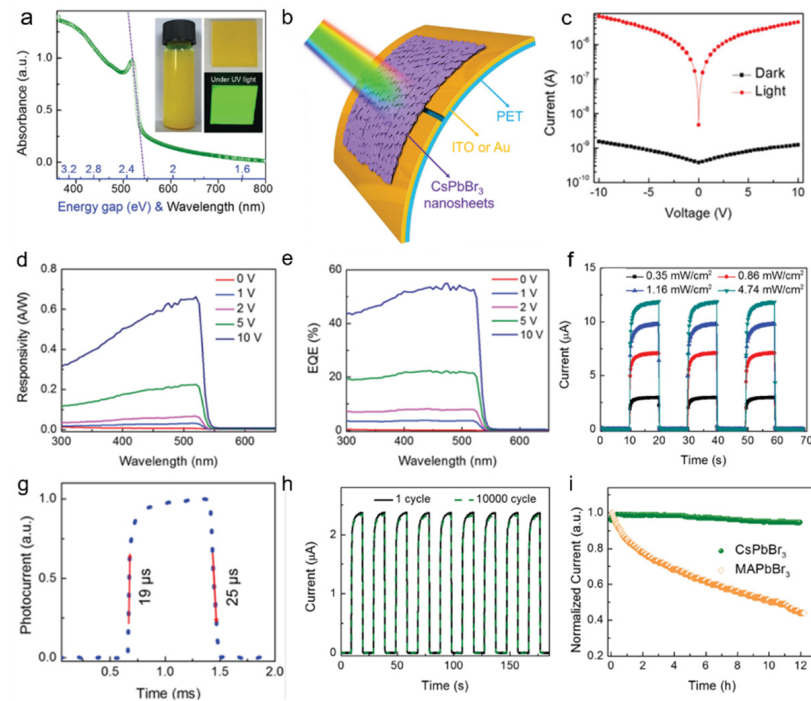


**Figure 2.** (a) UV-vis absorbance spectrum of CsPbBr<sub>3</sub> nanosheets. (b) The schematic of a flexible photodetector device based on the CsPbBr<sub>3</sub> nanosheet. (c) Logarithmic  $I-V$  characteristics of the photodetector in the dark and under irradiation with 442 nm light. (d) Responsivity and (e) EQE spectra of the photodetector. (f)  $I-t$  curves of the photodetector under 442 nm irradiation with different intensities. (g) Rise and decay times of the photodetector. (h) Photoresponse for the 1st and 10,000th bending-recovery cycle. (i) Excellent stability of photocurrent of CsPbBr<sub>3</sub> photodetectors. Reprinted with permission from ref. [43]. Copyright 2016 Wiley-VCH.

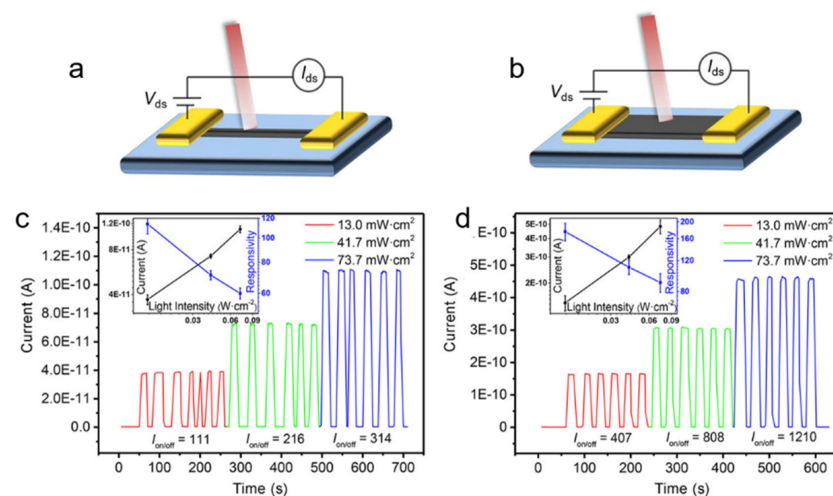


**Figure 3.** (a,b) Schematics of photodetectors based on an individual (a) nanowire crystal and (b) nanoplate crystal of MAPbI<sub>3</sub>. (c,d) Time response behavior of the photodetectors based on wire and platelet crystals, respectively. Reprinted with permission from ref. [53]. Copyright 2016 Wiley-VCH.

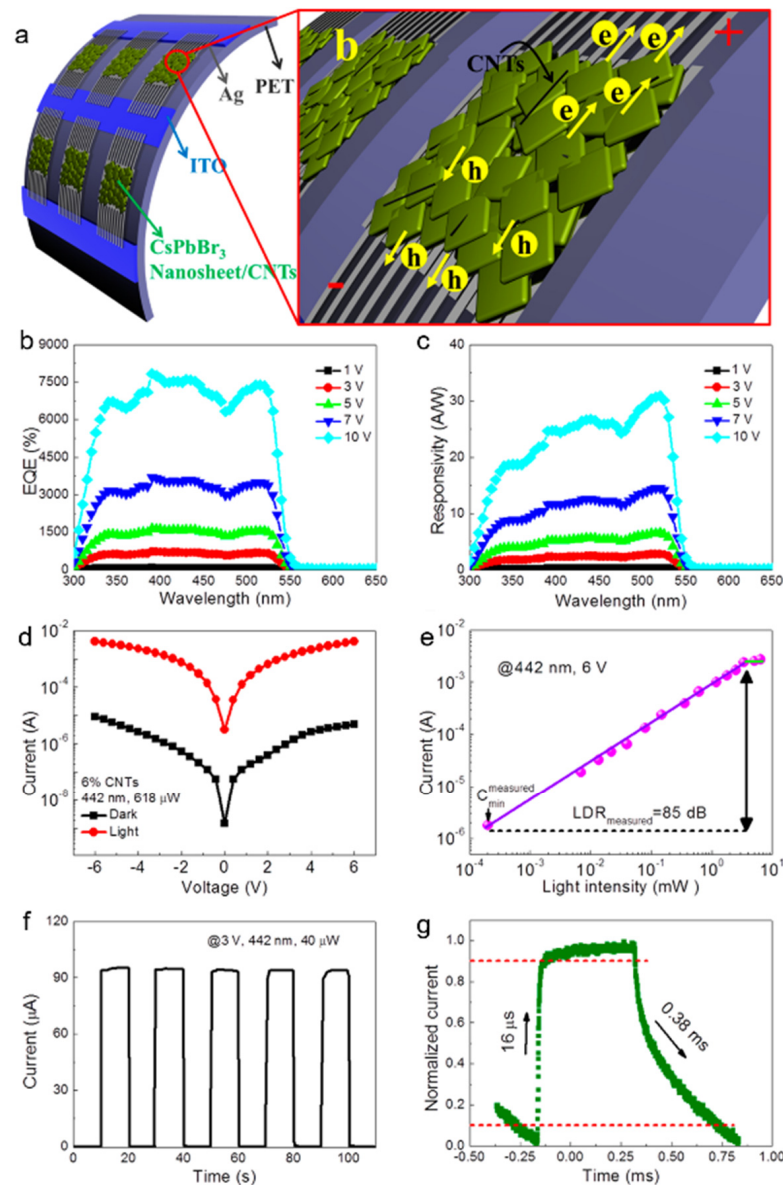


**Figure 4.** (a) Schematic illustration of the CsPbBr<sub>3</sub> nanosheet/ carbon nanotube (CNT)-based photodetector. (b) EQE and (c) responsivity spectra under different biases. (d) Logarithmic I–V curves under dark and 442 nm light illumination. (e) Photocurrent versus light intensity of the photodetector. (f) I–t curve of the photodetector. (g) Rise and decay time of the device. Reprinted with permission from ref. [55]. Copyright 2017 American Chemical Society.

### 2.1.2. Photoconductor Based on 1D Perovskites

Deng et al. [56] first reported photodetectors based on single-crystalline MAPbI<sub>3</sub> microwire (MW) arrays (Figure 5a). The device demonstrated an obvious response to visible light, but was rather insensitive to the UV and NIR light. (Figure 5b,c). High responsivity of 13.57 A W<sup>-1</sup> (Figure 5d), high detectivity of  $5.25 \times 10^{12}$  Jones and broad LDR (Figure 5e) were achieved in the MW array-based photodetectors. Compared with thin film-based photodetector, the MW array-based ones exhibit better stability by recording the dark and photocurrents of the photodetectors for 50 d (Figure 5f). The outstanding device performance can be attributed to the high optical absorption coefficient of MAPbI<sub>3</sub> and high crystallinity of the MWs.

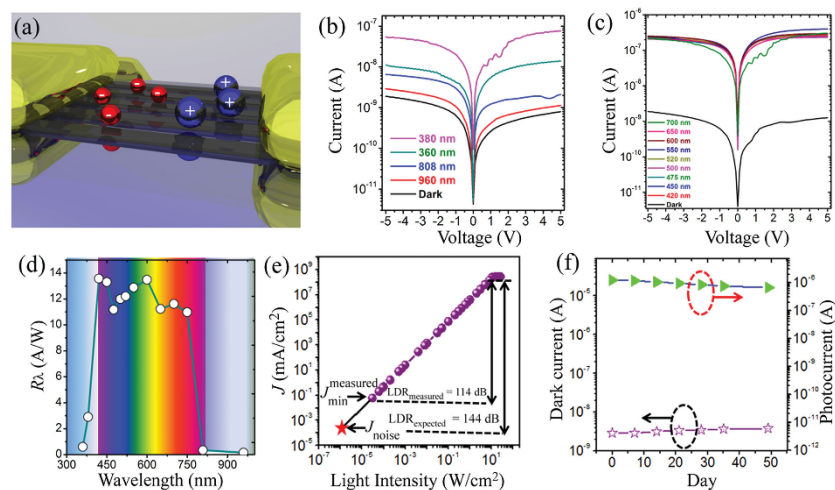


**Figure 5.** (a) Device structure of the MAPbI<sub>3</sub> microwire (MW) array-based photodetector. (b,c) I–V curves of a typical photodetector. (d) Photoresponsivity and photodetectivity of the MAPbI<sub>3</sub> MW array-based photodetector. (e) Photocurrent versus light intensity of the device under 550 nm light illumination. (f) Variation of dark current/photocurrent of MAPbI<sub>3</sub> MW arrays-based photodetector in ambient air. Reprinted with permission from ref. [56]. Copyright 2016 Wiley-VCH.

Li et al. [57] synthesized high crystalline MAPbI<sub>3</sub> MWs arrays by a solution-based blade coating and solvent recrystallization method. The corresponding schematic diagram of the as-fabricated photodetector was illustrated in Figure 6a. Apparently, the device exhibits a significant response to the UV and visible light, but is insensitive to the near-IR. (Figure 6b). The energy band diagram was shown in the inset of Figure 6c. Photoresponsivity of 0.04 AW<sup>-1</sup>, on/off ratio of  $0.84 \times 10^4$  and specific detectivity of  $0.6 \times 10^{12}$  Jones are shown in Figure 6e. The rise and decay time is 178/173 μs (Figure 6f). It is worth noting that the performance of the as-fabricated device has been significantly improved. The main reasons may be as follows: (i) High crystallinity and suitable surface roughness of the MAPbI<sub>3</sub> MWs are beneficial for the transport of carriers. (ii) The MAPbI<sub>3</sub> MWs and Ag electrodes form a stable and available Ohmic Contact. The results demonstrate that the MAPbI<sub>3</sub> MWs have a good application prospect in high-performance photodetectors.

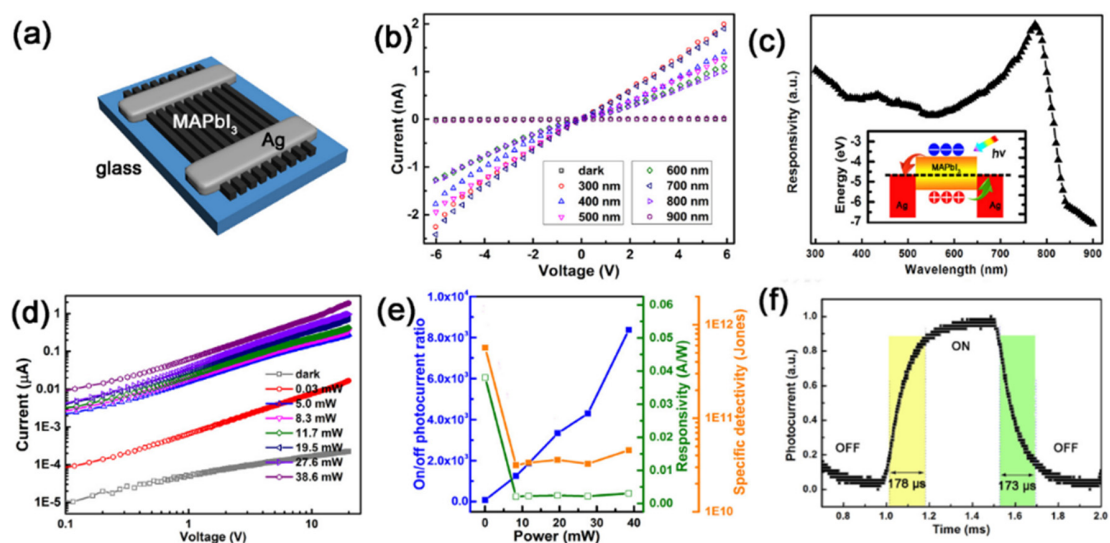


**Figure 6.** (a) The schematic diagram of the MAPbI<sub>3</sub> MWs-based photodetector. (b) I–V curves of the photodetector. (c) Wavelength-dependent responsivity of the photodetector. The inset is the energy band diagrams of the structure. (d) I–V curve of the photodetector with various light illumination power (650 nm). (e) On/off ratio, responsivity, and specific detectivity of the photodetectors. (f) Rise and decay time of the device. Reprinted with permission from ref. [57]. Copyright 2019 Elsevier.

By reacting Pb-containing precursor NWs with MABr and HBr in an organic solvent, Zhuo et al. [58] successfully prepared porous MAPbBr<sub>3</sub> NWs. The UV/Vis absorption spectrum (Figure 7a) indicates a favorable absorption capability with a direct band gap about 2.22 eV. A good ohmic contact was demonstrated by the typical linear and symmetrical I–V curve (Figure 7b). The on/off ratios of 61.9 suggested a good response to the light intensity. As shown in Figure 7d, the rise and decay times were 0.12 s and 0.086 s, respectively. The excellent photoelectric properties are mainly attributed to their unique 1D porous geometry, numerous active sites, and outstanding light absorption.

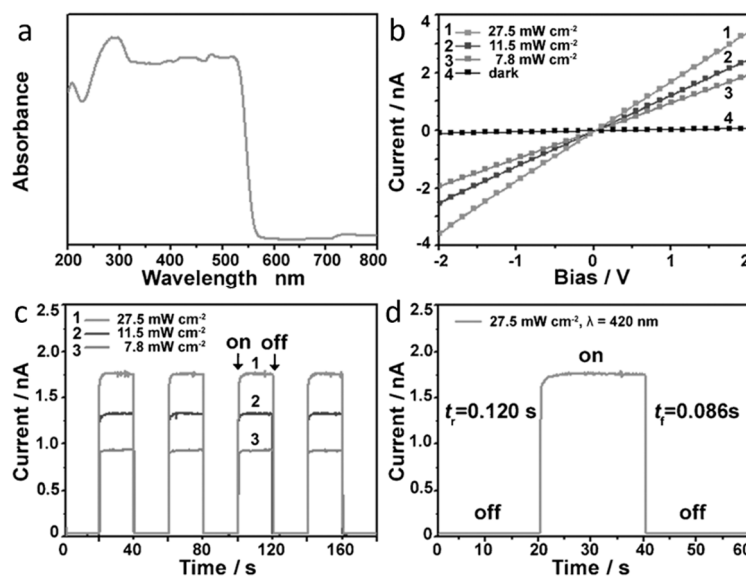


**Figure 7.** (a) UV/Vis absorption spectrum. (b) Typical I–V curves. (c,d) Photoresponse of the porous CH<sub>3</sub>NH<sub>3</sub>PbBr<sub>3</sub> nanowires (NWs). Reprinted with permission from ref. [58]. Copyright 2015 Wiley-VCH.

Deng et al. [59] reported high-quality single-crystalline MAPb(I<sub>1-x</sub>Br<sub>x</sub>)<sub>3</sub> ( $x = 0, 0.1, 0.2, 0.3, 0.4$ ) NWs with an absorption spectrum ranging from 680 to 780 nm by modifying I/Br ratio. The schematic diagram of the NWs-based device is shown in Figure 8a. The NWs-based photodetectors demonstrated an ultrahigh responsivity of  $1.25 \times 10^4$  A W<sup>-1</sup> due to the high-quality crystal structure of NWs (Figure 8c). In addition, other excellent figure-of-merit parameters were also obtained by the device, such as 3 dB bandwidth (0.8 MHz), large detectivity ( $1.73 \times 10^{11}$  Jones), LDR of 150 dB (Figure 8d), maximum G of 36,800 and robust stability. The high performance could be attributed to the long carrier lifetime and high carrier mobility in high-crystalline MAPbI<sub>3</sub> NWs. Thus, a variety of high-performance integrated optoelectronic devices could be fabricated by the NW arrays.

Tang et al. [60] successfully synthesized CsPb(Br/I)<sub>3</sub> nanorods with a facile hot-injection method. The PL and UV-vis absorption spectra indicate that the bandgap is  $\approx 1.98$  eV (Figure 9c). The schematic of the photodetector was illustrated in Figure 9a. The photosensitivity of the photodetector reaches  $10^3$ , and the rise and decay times were 0.68 s and 0.66 s, respectively (Figure 9d). Figure 9e indicated the photodetector meets well with the ohmic characteristics with a linear I–V curve. I–t curve demonstrated a remarkable high on/off ratio of 2000. The good performance of the photodetector can be related to the long lifetime and short transit time of the photocarriers in CsPb(Br/I)<sub>3</sub> nanorods with large surface-to-volume ratio and high density of deep level surface trap states.



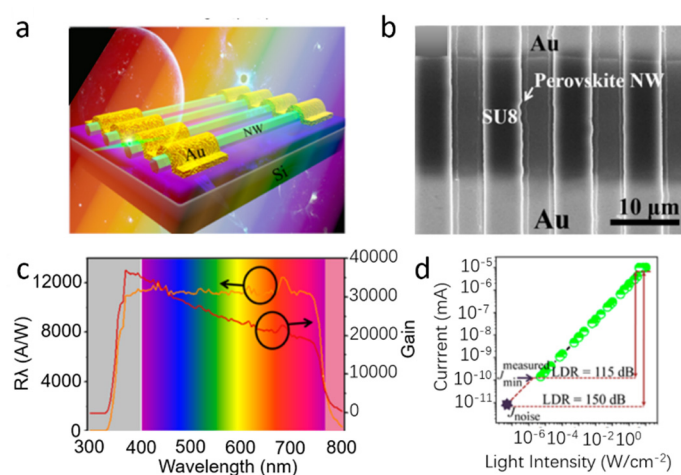


**Figure 8.** (a) Schematic of transistor based on the MAPbI<sub>3</sub> NWs. (b) SEM (scanning electron microscope) images of the phototransistor. (c) Responsivity and gain under different wavelength. (d) Dynamic response of the phototransistor. Reprinted with permission from ref. [59]. Copyright 2017 American Chemical Society.

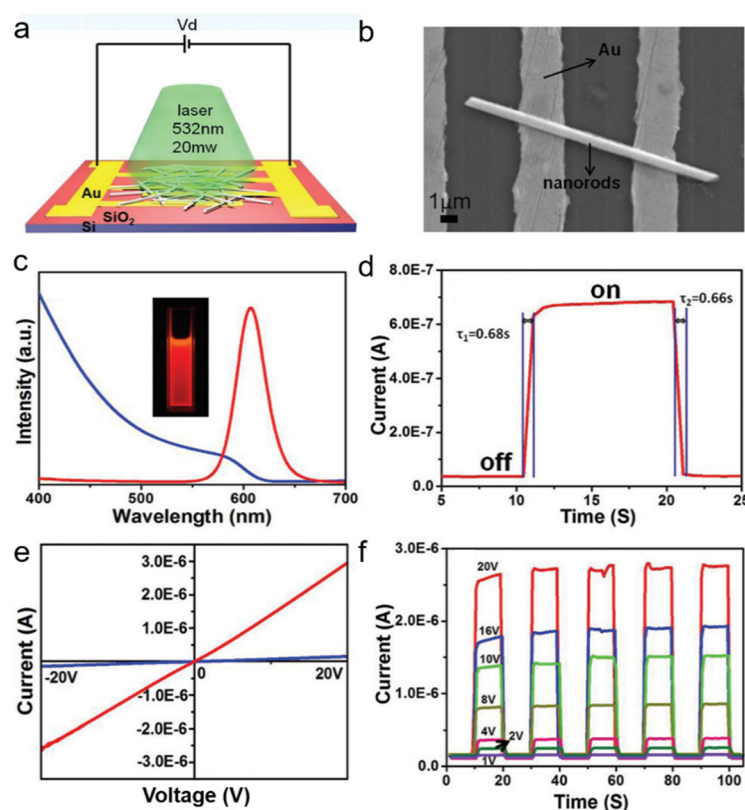


**Figure 9.** (a) The schematic of CsPb(Br/I)<sub>3</sub> nanorods-based photodetector; (b) SEM image of the device. (c) photoluminescence (PL) and absorption spectrum of the nanorods. (d) Rise and decay time of the photodetector. (e) I–V curve of the photodetector. (f) I–t curve as a function of bias voltages. Reprinted with permission from ref. [60]. Copyright 2016 Royal Society of Chemistry.

It is a common method to enhance the stability of perovskite by ligands to improve the performance of photodetector. Gao et al. [61] successfully synthesized MAPbI<sub>3</sub> NWs array by optimizing one-step self-assembly method. It turned out that the devices prepared by OA (Oleic acid)-passivated MAPbI<sub>3</sub> NWs have the best performance. The photodetector structure is schematically shown in Figure 10a. A broadband photoresponse range from 400 to 750 nm. The calculated responsivity is 0.45 AW<sup>-1</sup> (Figure 10b). The rising and

decay time are within 0.1 ms (Figure 10c). On/off ratio of 4000 reflects an excellent photosensitivity of the device (Figure 10d). Additionally, the ultralow dark currents result from low carrier density and low thermal emission (recombination) rates enable the device to detect very weak optical signals. In addition, the detectivity of  $2 \times 10^{13}$  Jones was achieved (Figure 10d). The improved performance can be attributed to the increasing of carrier lifetime after OA passivation, which can reduce the non-radiating composite centers on the surface of the NWs and gives the device more time to collect and transfer the photogenerated carriers.

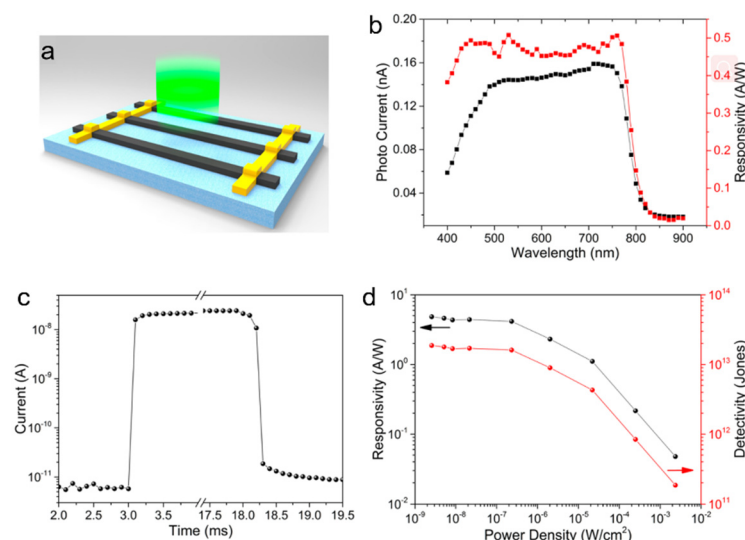


**Figure 10.** (a) Schematic of device structure of device. (b) Wavelength-dependent photocurrent and responsivity. (c) Transient response (current–time curve). (d) Light intensity dependent responsivity and detectivity. Copyright 2016, American Chemical Society [61].

To verify the influence of perovskite morphology on photodetector performance, Liu et al. [62] prepared MAPbI<sub>3</sub> with various morphology including NWs, microwires, a network, and islands by inkjet printing method with proper solvent and controlling the crystal growth rate. Photoconductor based on these different crystals were fabricated and among which, the MW-based photodetector exhibited better performance, such as a switching ratio of 16,000%, responsivity of 1.2 A/W, and normalized detectivity of  $2.39 \times 10^{12}$  Jones. The reason might be a more balance between the uniformity and low defects in MW MAPbI<sub>3</sub>. Both the rise time and decay time are within 10 ms (Figure 11c), which indicated the ability of MW MAPbI<sub>3</sub>-based photodetector to detect the rapidly changing optical signal.

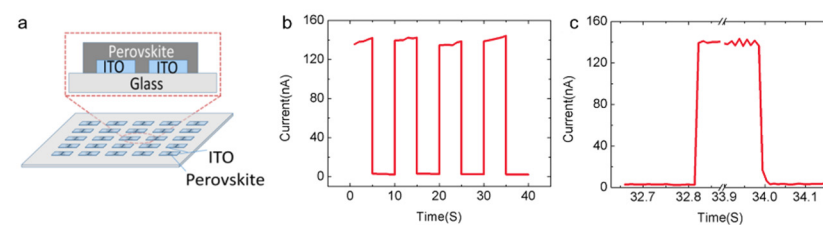


**Figure 11.** (a) Schematic of the photodetector. (b) Current-time curve of the MW-based photodetector. (c) Photoresponse time of the MW-based photodetector. Reprinted with permission from ref. [62]. Copyright 2019 American Chemical Society.

Chen et al. [42] synthesized  $\alpha$ -CsPbI<sub>3</sub> perovskite nanowire arrays with preferential (100) crystallographic orientation to further enhance the photodetector performance. High photoluminescence (PL) intensity (Figure 12a) and long PL lifetime (Figure 12b) demonstrated a low trap density in  $\alpha$ -CsPbI<sub>3</sub> NWs, which originates from their suppressed

grain boundaries and surface defects. High-performance photodetectors based on the as-fabricated NWs were constructed. The schematic diagram of photodetector was shown in the insert of Figure 12c. The photodetector exhibits high responsivity of  $1294 \text{ A W}^{-1}$  and detectivity of  $2.6 \times 10^{14}$  Jones (Figure 12d). The rise time is 0.85 ms, and the decay time is 0.78 ms (Figure 12f). The performance can maintain 90% after 30 days demonstrated an excellent long-term stability. The high performance mainly benefits from fewer grain boundaries and ordered crystallographic orientation.

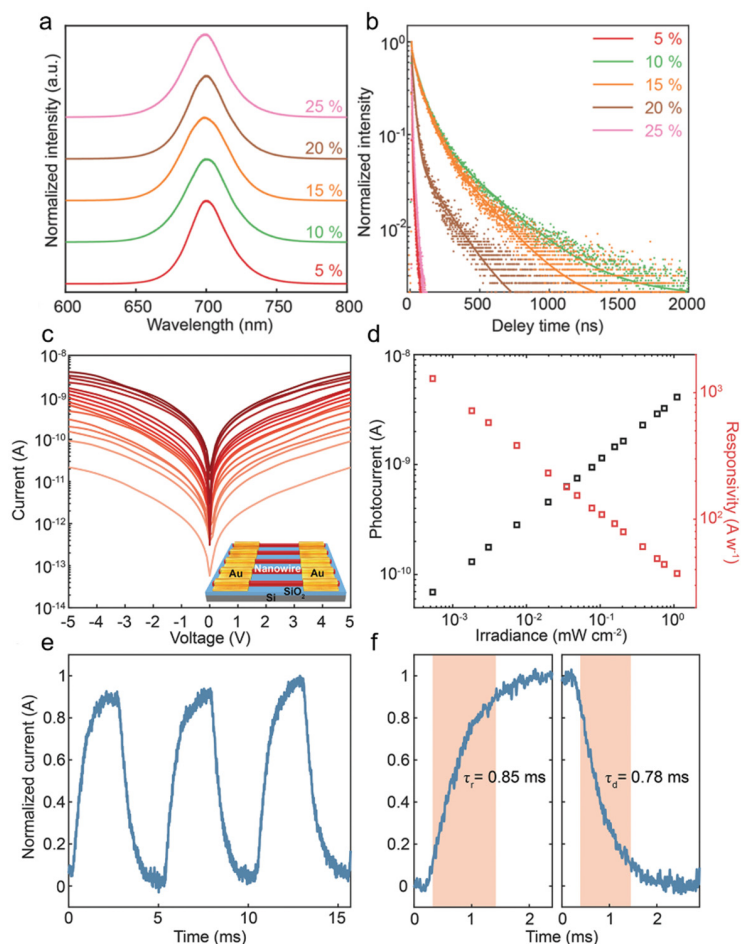


**Figure 12.** (a) Normalized PL emission, and (b) time-resolved PL spectra of CsPbI<sub>3</sub> NWs. (c) The typical I–V curves of  $\alpha$ -CsPbI<sub>3</sub> nanowire arrays, inset is the schematic illustration of device. (d) Photocurrent and responsivity of photodetector. (e) I–t response and (f) photoresponse time of photodetectors. Reprinted with permission from ref. [42]. Copyright 2019 Wiley-VCH.

In order to reduce the toxicity of lead to future applications, Han et al. [63] fabricated lead-free all-inorganic CsSnX<sub>3</sub> (X = Cl, Br, I) perovskite NW arrays on a mica substrate with the growth direction of [100] by Chemical vapor deposition. Uniform and strong PL peak suggested a high crystallinity. Furthermore, the narrow band gap of CsSnI<sub>3</sub> NW array extends the optoelectronic applications of perovskites from visible to near-infrared region and the as-fabricated photodetector based on CsSnI<sub>3</sub> NW array is the first reported near-infrared detector. The performance of the CsSnI<sub>3</sub> NW array-based photodetector is shown in Figure 13. The maximum responsivity occurred at 940 nm, so the photodetector is irradiated with 940 nm laser (Figure 13a). The photocurrents increase with the increase of the incident intensity and excellent stability and reproducibility were shown in Figure 13b. The rise and decay time were 83.8 and 243.4 ms, respectively. The fast photoresponse can be attributed to the high-quality of CsSnI<sub>3</sub> NW array with less surface states and trap centers. The responsivity and detectivity were  $54 \text{ mA W}^{-1}$  and  $3.85 \times 10^5$  Jones, respectively.

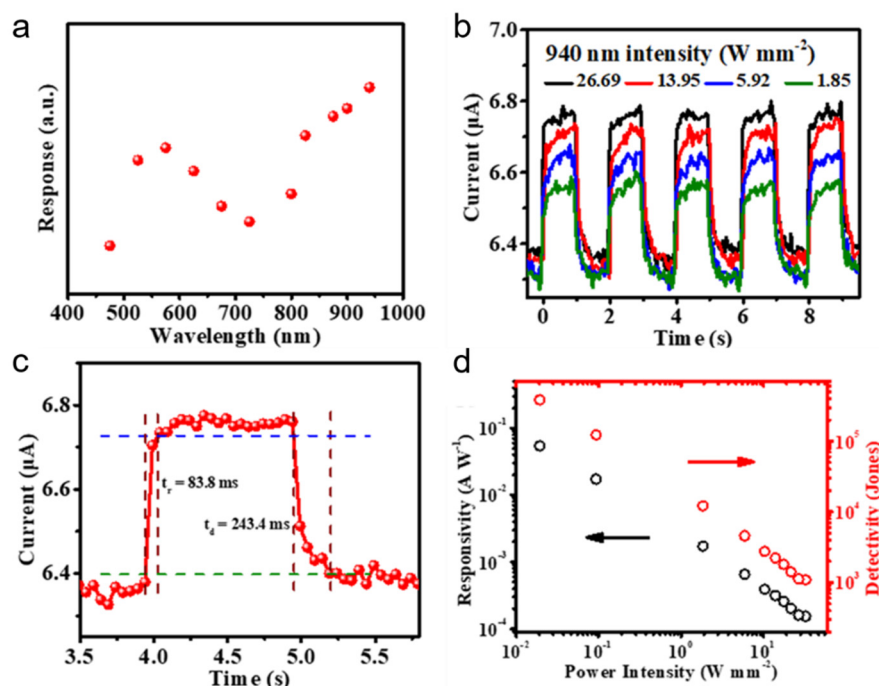


**Figure 13.** Near-infrared photodetection performance of CsSnI<sub>3</sub> NW array-based photodetector. (a) Spectral response of the photodetector illuminated from 475 to 940 nm. (b) Time-response curves of photodetector. (c) Rise and decay time constants. (d) Responsivity and detectivity of the photodetector. Reprinted with permission from ref. [63]. Copyright 2019 Scientific Publishers of India.

Li et al. [64] constructed a polarization-sensitive UV photodetector based on another all-inorganic perovskite CsCu<sub>2</sub>I<sub>3</sub> NW (Figure 14a). Anisotropy ratio of PL intensity can be up to 3.16 (Figure 14c). The schematic diagram of a photodetector based on CsCu<sub>2</sub>I<sub>3</sub> NW was shown in Figure 14d. As shown in Figure 14e, the device can respond to light from 230 to 350 nm. The asymmetrical *I*–*V* curves demonstrated the formation of a Schottky barrier (Figure 14f). The performance of photodetector based on CsCu<sub>2</sub>I<sub>3</sub> NW is impressive, such as a high on/off ratio of  $2.6 \times 10^3$  (Figure 14g), a photoresponsivity of  $\sim 32.3 \text{ AW}^{-1}$ , a high specific detectivity of  $1.89 \times 10^{12}$  Jones (Figure 14h), and a fast response speed of 6.94/214  $\mu\text{s}$  (Figure 14i). In addition, a good flexibility and stability had been demonstrated by 1000 bending cycles without no photoresponse degradation (Figure 14j).

### 2.1.3. Photoconductor Based on Other Nanostructured Perovskites

Dong et al. [65], for the first time, fabricated a photodetector based on the all-inorganic perovskite CsPbBr<sub>3</sub> nanocrystals (NCs) with synergetic effect of preferred-orientation and plasmonic effect. The schematic diagram of the device is shown in Figure 15a. Figure 15b indicated a broadband photodetection range from 300 to 520 nm. The peak responsivity value is 20.92  $\text{mA W}^{-1}$ . The increase below 520 nm is attributed to the increased concentration of electron–hole pairs. The light on/off ratio is  $>1.6 \times 10^5$ , as shown in Figure 15c. Figure 15d exhibited stable and reproducible photoresponse. The rise and decay time were 0.2 and 1.3 ms, respectively (Figure 15e).

Ramasamy et al. [52] chose red emitting CsPbI<sub>3</sub> NCs to fabricate photoelectronic devices because a relatively longer radiative lifetime than the green and blue emitting in CsPbX<sub>3</sub> (X = Cl, Br) NCs helps to generate large photocurrent. The schematic diagram of the CsPbI<sub>3</sub>-based photodetector is shown in Figure 16a. The as-fabricated photodetector exhibits a high performance, including high photosensitivity of  $10^5$  (Figure 16b), reproducible response to ON/OFF cycles (Figure 16c), fast response time of 24/29 ms (Figure 16d), which make a promising application in photoelectric devices.

Algadi et al. [66] constructed nitrogen doped graphene quantum dots (GQDs)/CsPbBr<sub>3</sub> NCs photodetectors, in which the GQDs act as an electron transfer layer, while the CsPbBr<sub>3</sub>

as light absorber. Figure 17a presents the schematic diagram of the hybrid photodetector. As shown in Figure 17b, the PL lifetime of the QDs-passivated CsPbBr<sub>3</sub> NCs is obviously decreased, demonstrating a great deal of charge transfer at the QDs/CsPbBr<sub>3</sub> interface. The heterostructure-based photodetector exhibits a higher performance than pure one, such as higher on/off ratio of  $7.2 \times 10^4$  (Figure 17c), higher photoresponsivity of  $0.24 \text{ AW}^{-1}$  (Figure 17d), larger specific detectivity of  $2.5 \times 10^{12}$  Jones, EQE of 57% (Figure 17e), shorter decay time as 1.16 ms (Figure 17f).

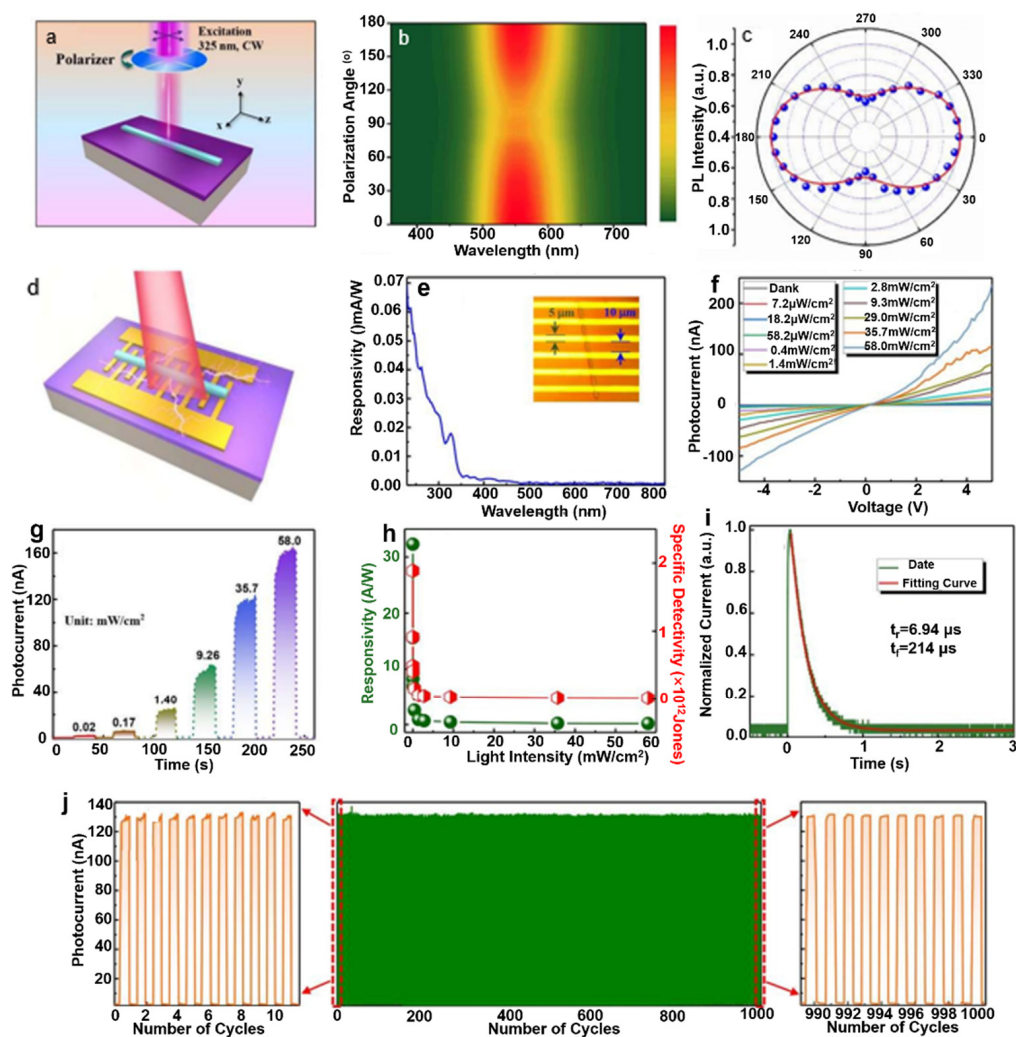


**Figure 14.** (a) Schematic diagram of polarization PL measurements. (b) PL spectra vs. incident light polarization. The color represents the emission intensity. (c) Polarization-dependent PL intensity of CsCu<sub>2</sub>I<sub>3</sub> NWs. (d) Schematic diagram of the CsCu<sub>2</sub>I<sub>3</sub> NW-based photodetector. (e) Responsivity for different incident wavelength. Inset is the optical microscope image of the photodetector. (f) I–V and (g) I–t curves of the photodetector with different incident power. (h) Responsivity and specific detectivity with different incident power. (i) Rise and decay time of the photodetector. (j) Photoresponse maintained well after 1000 bending cycles. Reprinted with permission from ref. [64]. Copyright 2020 Royal Society of Chemistry.

## 2.2. Phototransistor

### 2.2.1. Phototransistor Based on 2D Perovskites

The above experimental results show that it is difficult to obtain high responsivity and fast response speed simultaneously by using photoconductive device. The phototransistor can achieve a balance between the responsivity and response speed by modulating the gate voltage.

Liu et al. [67] constructed a field-effect transistor (FET) based on 2D MAPbX<sub>3</sub> nanosheet prepared by a combined solution process and vapor-phase conversion method. The schematic diagram of the FET device is shown in Figure 18a. Figure 18b shows the picture and PL mapping images of the FET. The photocurrent under dim light promises great potential as an effective photodetector. The linear I–V curves (Figure 18c) indicate the contact between 2D MAPbX<sub>3</sub> nanosheet and gold electrodes is ohmic. The on/off ratio of the FET can reach up to 10<sup>2</sup> (Figure 18c, inset), which can be related to strong light–matter interaction and absorptive capacity of 2D MAPbX<sub>3</sub> nanosheet. I–t curve further demonstrated an effective optical switching, as shown in Figure 18d. The responsivity of the FET was calculated to be 22 AW<sup>−1</sup> (Figure 18e). Rise and decay times of the FET are within 20 and 40 ms, respectively (Figure 18f). The results demonstrate that the 2D perovskite photodetector has excellent photoresponsivity and relatively fast response speed.

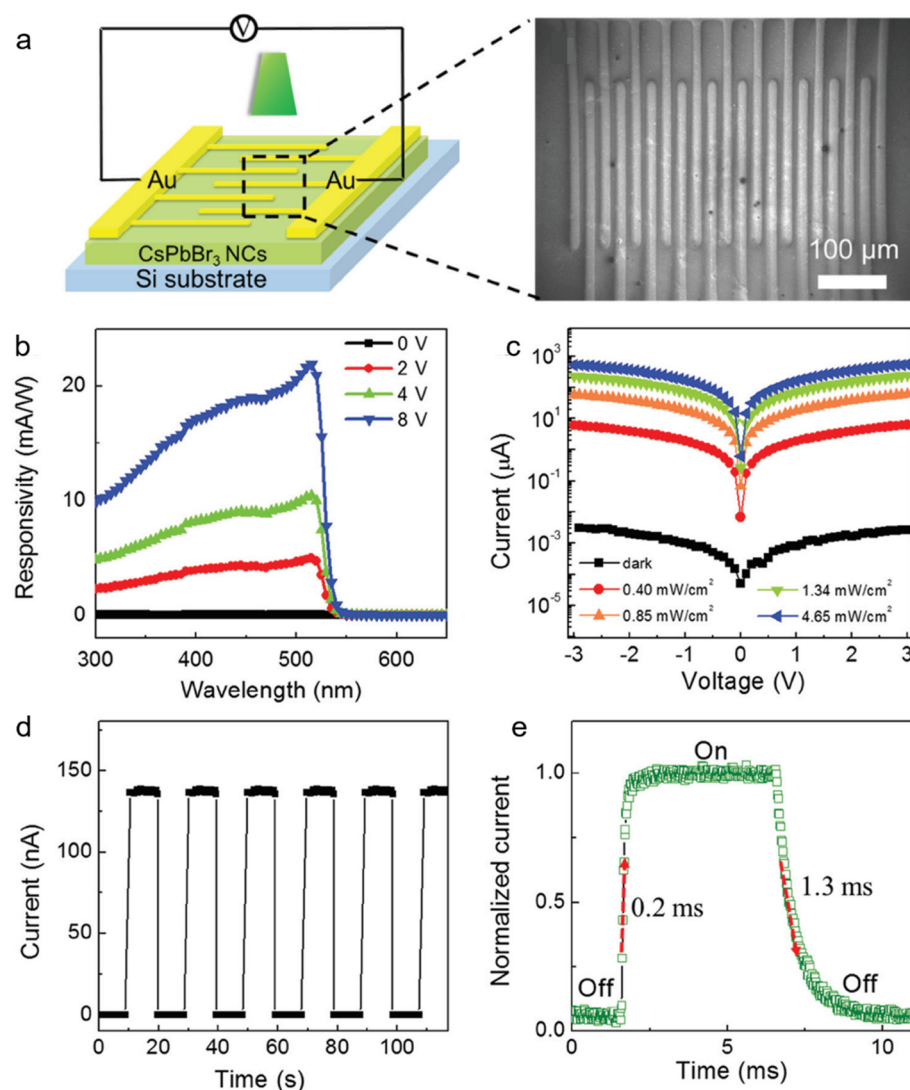


**Figure 15.** (a) Schematic and microscope image of CsPbBr<sub>3</sub> NC-based photodetector. (b) Responsivity of the photodetector. (c) I–V curves of photodetector with different light irradiation intensity. (d) I–t curve of photodetector. (e) Rise and decay time of the device. Reprinted with permission from ref. [65]. Copyright 2016 Wiley-VCH.

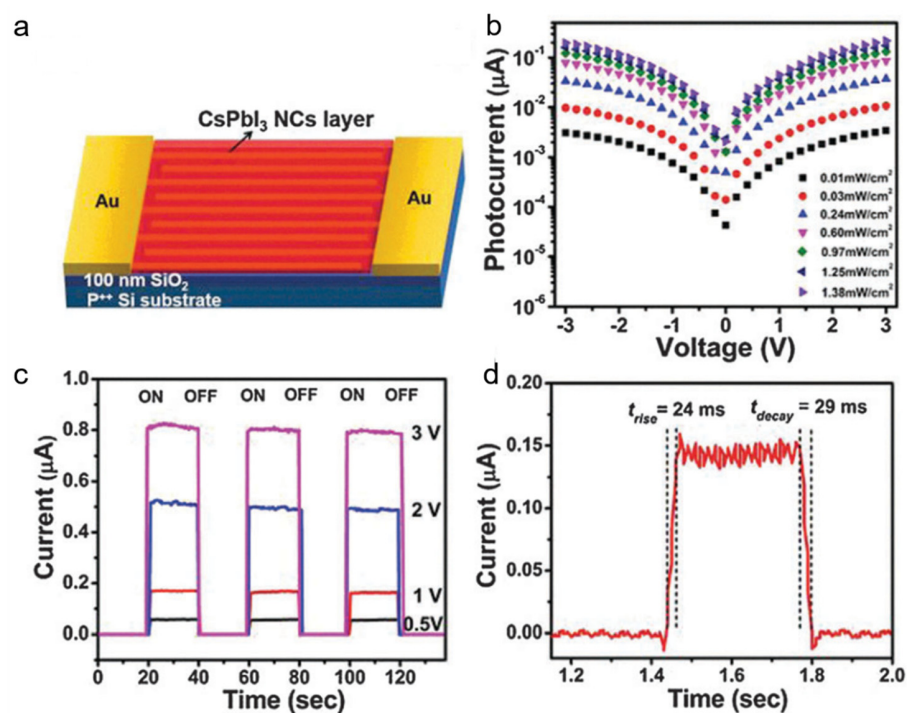


**Figure 16.** (a) Schematic diagram of the CsPbI<sub>3</sub> nanocrystals (NCs)-based photodetector. (b) I–V curve of photodetector with incident light intensity. (c) I–t curve as a function of applied bias. (d) Rise and decay time of the device. Reprinted with permission from ref. [52]. Copyright 2016 Royal Society of Chemistry.

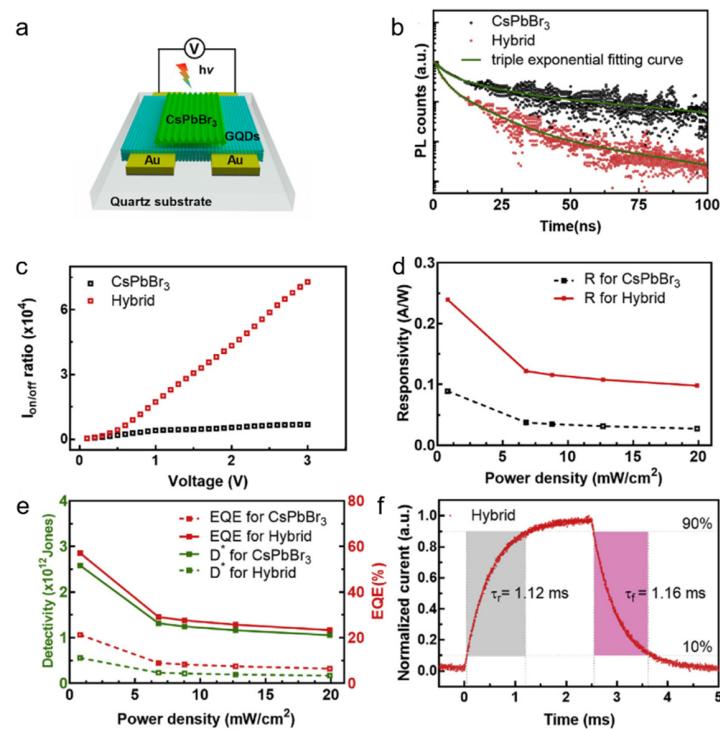


**Figure 17.** (a) Schematic diagram of the graphene quantum dots (GQDs)/CsPbBr<sub>3</sub>-based photodetector. (b) Time-resolved PL decay transients for the pure and hybrid structures. (c) On/off ratio, (d) Photoresponsivity, (e) specific detectivity ( $D^*$ ), and EQE of the pure CsPbBr<sub>3</sub>-based and hybrid photodetectors. (f) Rise and decay time of the hybrid photodetector. Reprinted with permission from ref. [66]. Copyright 2020 Elsevier.

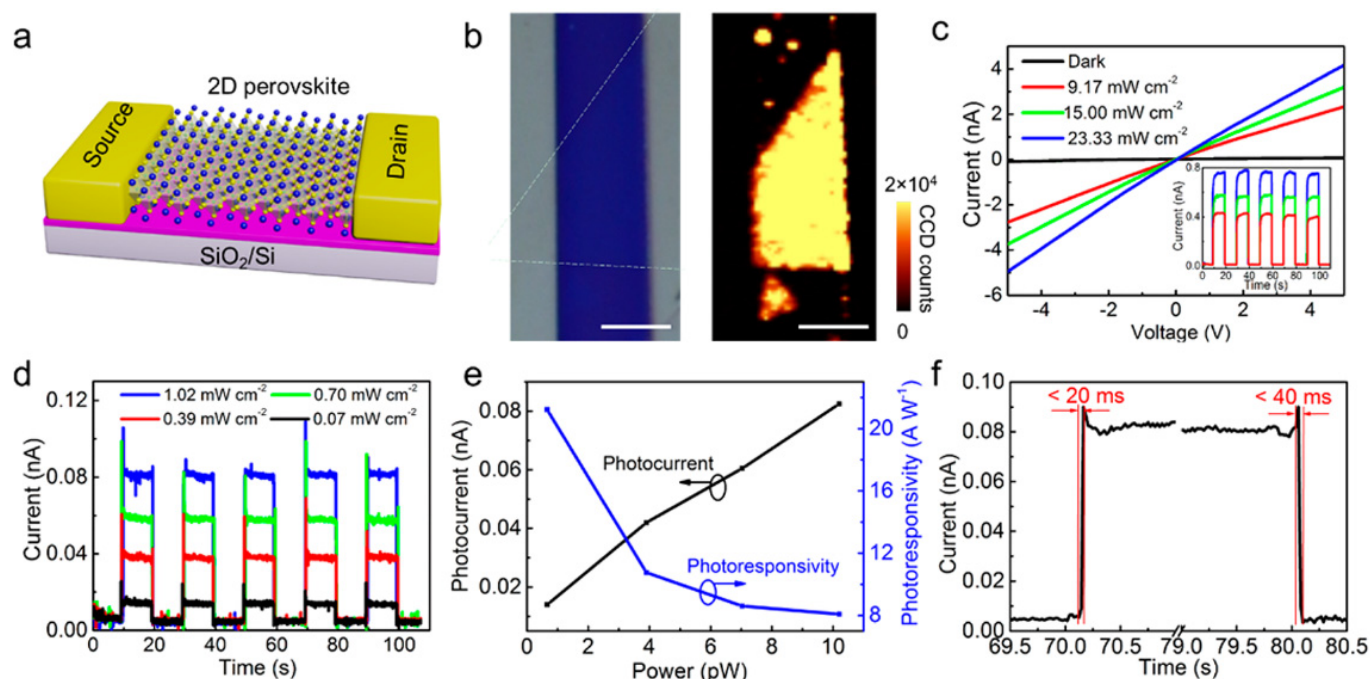


**Figure 18.** (a) Schematic diagram of a phototransistor based on 2D MAPbX<sub>3</sub> nanosheet. (b) Picture (left) and PL mapping image (right) of field-effect transistor (FET). (c) I–V curves of the FET. Inset: I–t curve under different power with a voltage bias of 1 V. (d) I–t curve of the FET under the different power. (e) Photocurrent and responsivity as a function of incident power. (f) Rise and decay times of the FET are within 20 and 40 ms, respectively. Reprinted with permission from ref. [67]. Copyright 2016 American Chemical Society.

Lv et al. [68] fabricated a FET based on 2D all-inorganic CsPbBr<sub>3</sub> nanosheet to investigate photoelectronic performance. The schematic was illustrated in Figure 19a. I–V curve with a significantly increased photocurrent (Figure 19b) demonstrates that 2D CsPbBr<sub>3</sub> nanosheet has a great potential to be an efficient photodetector. The fast and reproducible on/off cycle exhibit an excellent photo switching and stability of the as-fabricated photodetector (Figure 19c). The rise time was 17.8 ms, and the decay times were determined to be 14.7 and 15.2 ms (Figure 19d).

### 2.2.2. Phototransistor Based on 1D Perovskites

In 2014, Horvath et al. [69] reported the first MAPbI<sub>3</sub> NWs-based photodetectors. Figure 20a,b showed the schematic diagram and the microscope image of the device, respectively. The linear output characteristics indicate that the contacts between MAPbI<sub>3</sub> NWs and electrodes are ohmic (Figure 20c). The current increases parabolically with the incident power, but the photocurrent does not reach saturation (inset to Figure 20c). Responsivity was calculated to be 5 mA/W. The rise and decay time were 0.35 ms and 0.25 ms, respectively, demonstrated a fast response behavior in the photodetector (Figure 20d). In addition, the EQE of the perovskites MWs-based device is twice as high as nanoparticles-based one, which demonstrated the morphological properties could play an essential role in photodetection.



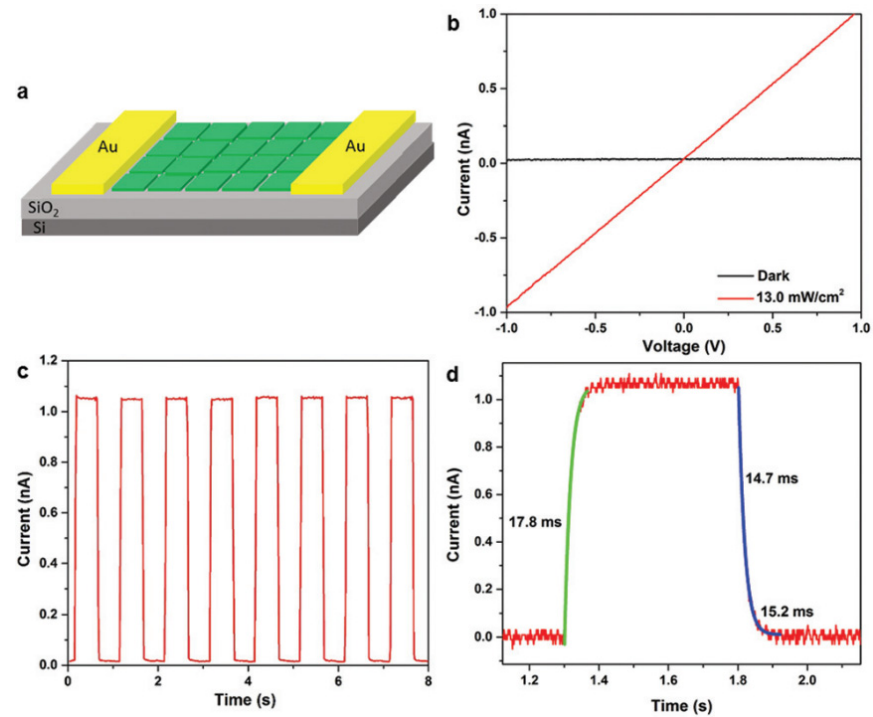


**Figure 19.** (a) Schematic diagram of the phototransistor based on CsPbBr<sub>3</sub> nanosheets. (b) I–V curves of the photodetector. (c) I–t curve of the photodetector. (d) Rise and decay times of the photodetector. Reprinted with permission from ref. [68]. Copyright 2016 Royal Society of Chemistry.

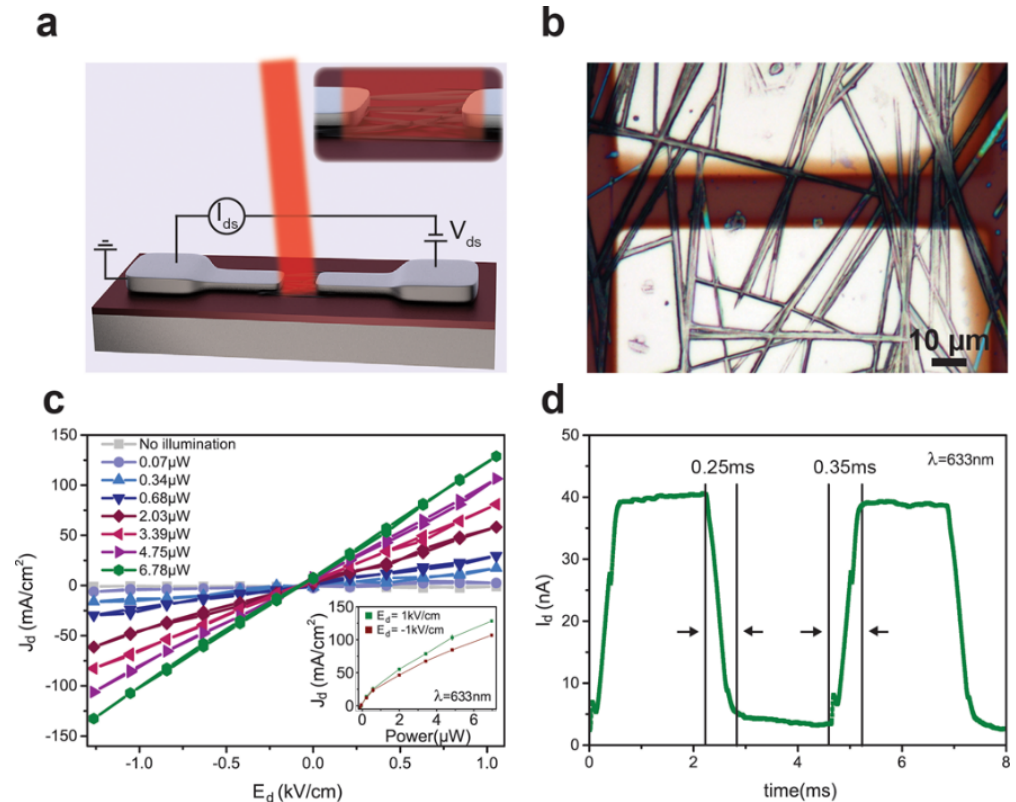


**Figure 20.** (a) Schematic diagram of the MAPbI<sub>3</sub> NWs-based FET and I–V photocurrent measurements. (b) Microscopy image of the FET based on MAPbI<sub>3</sub> NWs. (c) Dark and laser illuminated I–V curves as a function of laser power. (d) Rise and decay time of the FET. Reprinted with permission from ref. [69]. Copyright 2014 American Chemical Society.

Zhu et al. [70] constructed a FET based on MAPbI<sub>3</sub> MWs to study photoelectronic characteristics. The schematic diagram of FET is shown in Figure 21a. SEM image of the FET based on MAPbI<sub>3</sub> microwires was shown in the inset of Figure 21a. The on-off ratio was calculated to be  $4.02 \times 10^3$  (Figure 21b). A stable and reproducible I-t curve demonstrated the fast response and stability of the MAPbI<sub>3</sub> MWs-based device (Figure 21c). Good performance should be beneficial to the carrier charge transport caused by the oriented alignment of the microwires and narrow electrode channel distance of about 20 nm. In addition, a stable and available ohmic contact make contributions as well. The rise and decay time was 0.2 ms and 0.25 ms, respectively (Figure 21d). The relatively low responsivity of  $0.3 \text{ A W}^{-1}$  may be caused by low efficient electron transfer during the light absorption.

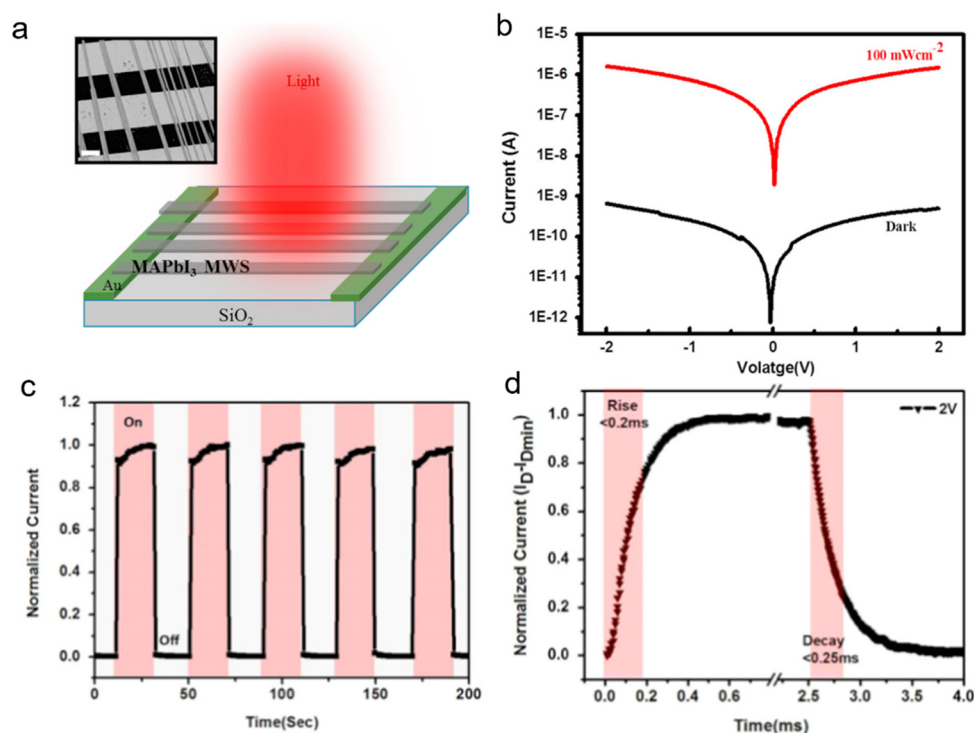


**Figure 21.** (a) Schematic diagram of the FET based on MAPbI<sub>3</sub> MWs, inset: SEM image of the FET. (b) I–V curve of the photodetector under dark and illumination at  $100 \text{ mWcm}^{-2}$ . (c) I–t curves of the photodetector. (d) Rise and decay time were 0.2 ms and 0.25 ms, respectively. Reprinted with permission from ref. [70]. Copyright 2016, Elsevier.

Xiao et al. [71] fabricated a phototransistor based on MAPbI<sub>3</sub> NWs with well-defined facets and smooth surfaces. The SEM image of the device was shown in Figure 22a. Under illumination, the I–V<sub>sd</sub> curves are nonlinear, and the current reaches saturation at high V<sub>sd</sub> (Figure 22b), which indicates a diode contact barrier. At high V<sub>sd</sub>, the saturation region exhibits a linear laser power-photocurrent curve (Figure 22c). The responsivity R was calculated to be  $0.11 \text{ AW}^{-1}$ . A gain was estimated to be 0.25. In addition, they demonstrated that the photocurrent becomes stronger as the excitation energy close to the bandgap due to the strong light coupling, which provides new insights to the carrier transport and dynamics.

Spina et al. [72] fabricated a phototransistor based on MAPbI<sub>3</sub> NWs/monolayer graphene to improve the performance of the pure MAPbI<sub>3</sub>-based photodetector by using high carrier mobility in graphene. Schematic diagram was shown in Figure 23a. In this device, positive charge carriers were injected into the graphene and negative charges accumulated in the NWs. The accumulating negative charges serve as an additional light tunable gate, further reducing the Fermi energy of graphene (Figure 23b). The key role

of MAPbI<sub>3</sub> NWs in the photon-induced carrier generation can be revealed by spectral sensitivity (Figure 23c). The responsivity reaches up to  $2.6 \times 10^6$  A W<sup>-1</sup> (Figure 23e). The rise and decay time were 55 s and 75 s, respectively (Figure 23f). As the size of the device is reduced by 5-fold, the photoresponse is increased by about 10-fold. It should be contributed to the more effective collection of the photogenerated charge carriers.

Chen et al. [73] fabricated a phototransistor based on the C8BTBT/CsPbI<sub>3</sub> nanorod heterojunction. Figure 24a illustrated the schematic of the phototransistor. The I<sub>D</sub>-V<sub>D</sub> curve of the phototransistor exhibit both linear and saturation regions (Figure 24b,c). The transfer curves (I<sub>D</sub>-V<sub>G</sub>) as shown in Figure 24d show a typical p-type semiconductor behavior. The photocurrent shows that the larger gate voltage applied, the faster photocurrent increased (Figure 24e). The responsivity of  $4.3 \times 10^3$  A W<sup>-1</sup> was obtained, as shown in Figure 24f. The on/off ratio was calculated to be  $2.2 \times 10^6$  as shown in Figure 24g. More importantly, due to the high stabilities of the two materials and device structure, the hybrid phototransistors possessed long-term stabilities under ambient conditions.

Meng et al. fabricated a phototransistor based on CsPbX<sub>3</sub> (X = Cl, Br, or I) NWs with a uniform diameter of ~150 nm. As shown in Figure 25, these devices exhibit high performance with the responsivity exceeding 4489 A/W and detectivity over  $7.9 \times 10^{12}$  Jones. The response times are found to be less than 50 ms. The excellent performance can be attributed to the reduced defect concentration in CsPbX<sub>3</sub> NWs as well as the field-effect transistors (FET) with superior hole field-effect mobility of 3.05 cm<sup>2</sup>/(V s) [74].

Yang et al. constructed a phototransistor based on CsPbI<sub>3</sub> nanorods. The schematic diagram of the device was shown in Figure 26a. The linear and symmetric I-V curves demonstrated that the contact was ohmic, as shown in Figure 26b. The as-fabricated device exhibited a totally excellent performance, such as high responsivity of  $2.92 \times 10^3$  A·W<sup>-1</sup>, large EQE of  $0.9 \times 10^6\%$ , fast response time of 0.05 ms, and a high detectivity of  $5.17 \times 10^{13}$  Jones (Figure 26c–f). The excellent performance is mainly due to the following two reasons. First, high absorption coefficient, low recombination of charge carriers and low density of defects of CsPbI<sub>3</sub> nanorods generate strong photoelectric effect. Second, the high-quality nanorod provides a smooth and short path for carrier transfer, and significantly improves the response speed [75].

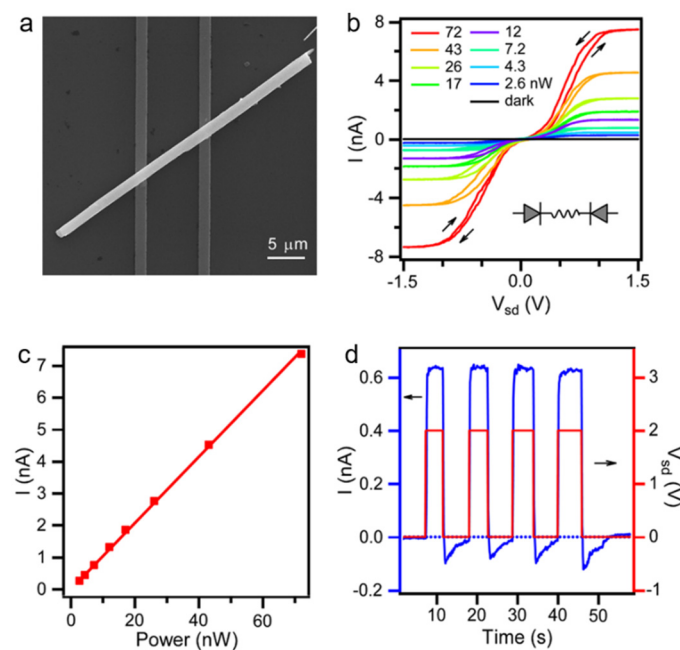


**Figure 22.** (a) SEM image of the MAPbI<sub>3</sub> NM-based photodetector. (b) I-V<sub>sd</sub> curves of the device. (c) Laser-power-dependent photocurrent in the saturation region at high V<sub>sd</sub>. (d) I-t curves of the photodetector. Reprinted with permission from ref. [71]. Copyright 2016 American Chemical Society.

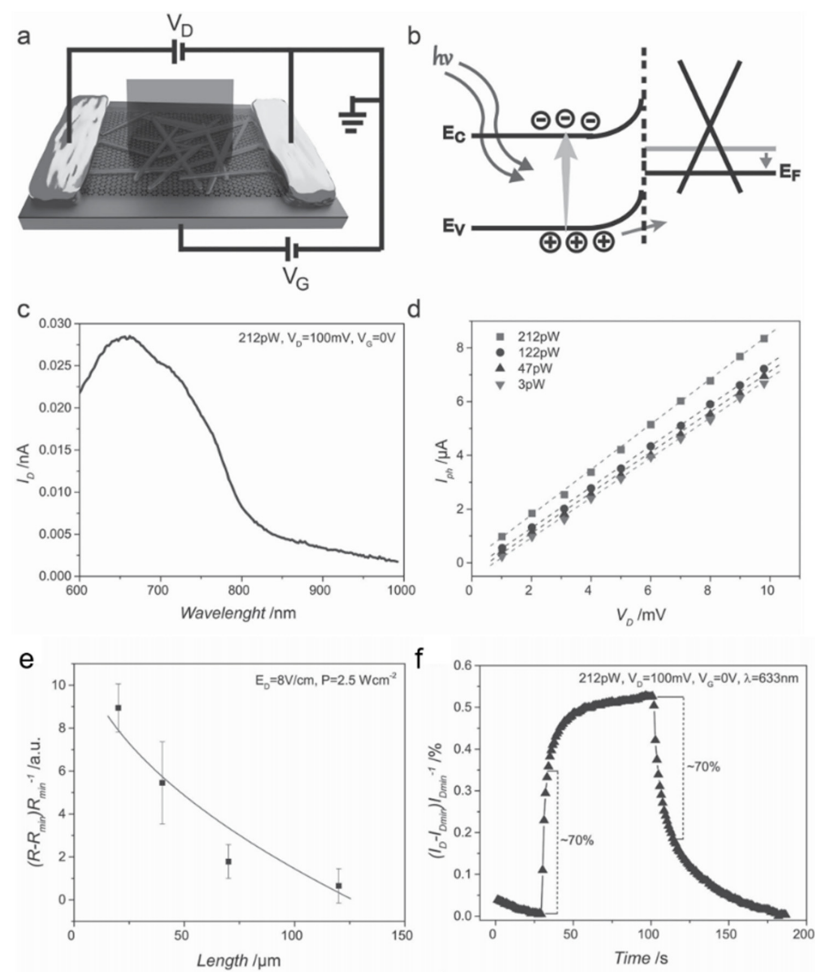


**Figure 23.** (a) Schematic diagram of the phototransistor based on MAPbI<sub>3</sub> NWs/monolayer graphene. (b) The band diagram of the MAPbI<sub>3</sub> NW/graphene heterojunction. (c) Wavelength-dependent photocurrent. (d) I–V curves of the photodetector. (e) The responsivity as a function of the device length. (f) Time response of the phototransistor. Reprinted with permission from ref. [72]. Copyright 2015 Wiley-VCH.

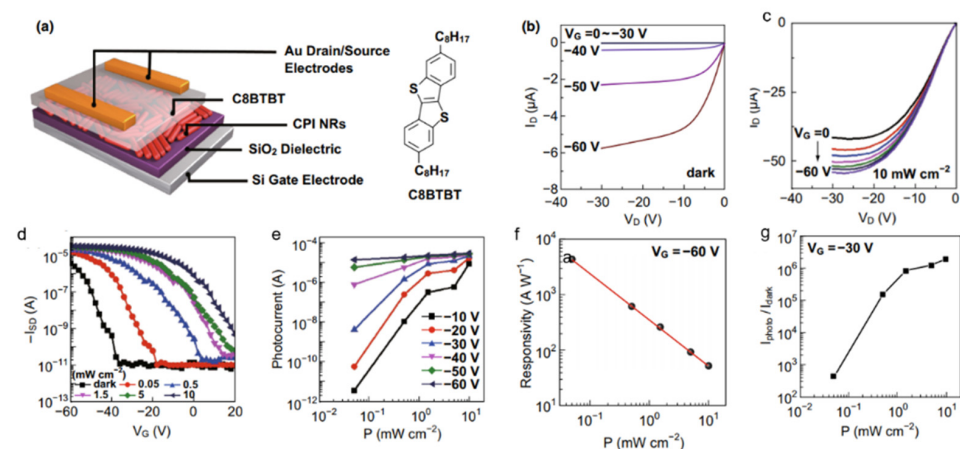


**Figure 24.** (a) Schematic diagram of phototransistor based on C8BTBT/CsPbI<sub>3</sub> nanorod heterojunction. ID–VD transistor characteristics in the dark state (b) and under a white-light illumination (c). (d) Transfer characteristics ( $V_D = -30$  V) under different incident power. (e) Photocurrent as a function of the incident power under different gate voltages. (f) Responsivity as a function of incident power. (g) On/off ratio as a function of incident power. Reprinted with permission from ref. [73]. Copyright 2018 Springer Singapore.

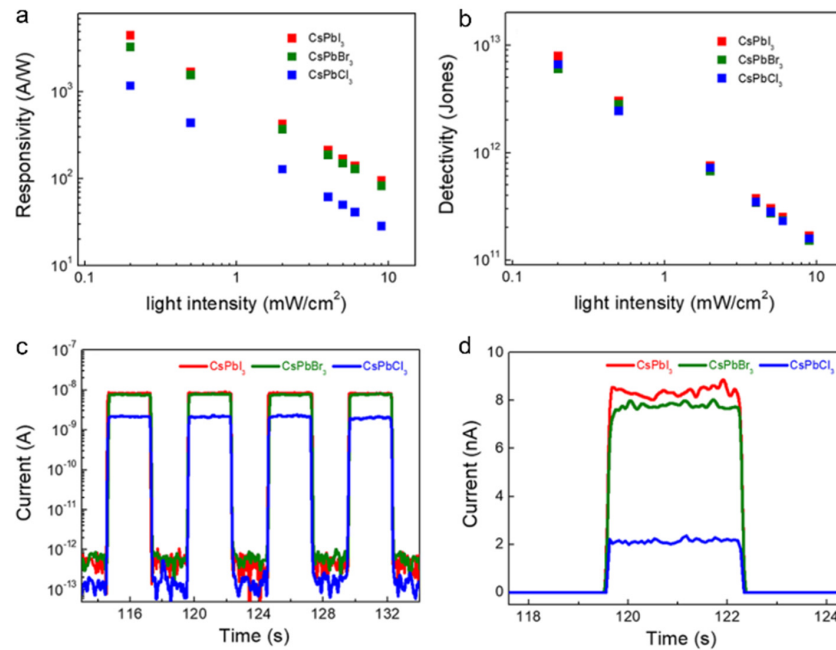


**Figure 25.** (a,b) Responsivity and detectivity vs. light intensity. (c,d) I–t curve under illumination ( $9 \text{ mW/cm}^2$ ) and a bias voltage of 5 V. Reprinted with permission from ref. [74]. Copyright 2019 American Chemical Society.

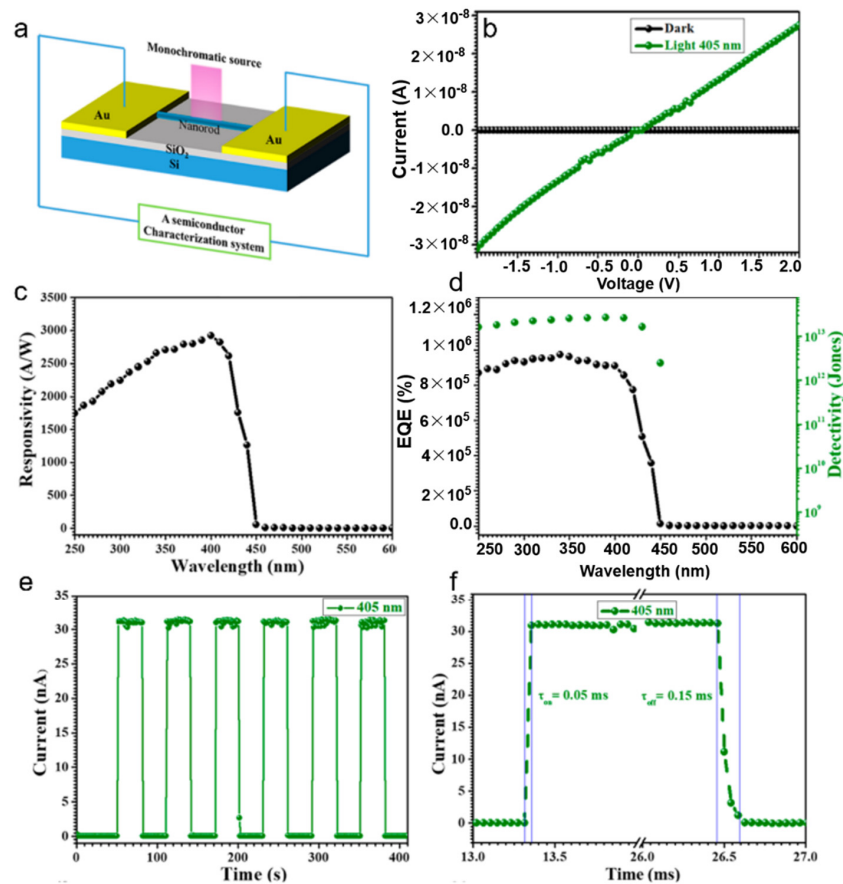


**Figure 26.** (a) Schematic diagram of the as-fabricated phototransistor based on a single  $\text{CsPbI}_3$  nanorod. (b) I–V characteristics under dark and 405 nm irradiation. (c,d) Representative, EQE and Detectivity vs. wavelength. (e,f) I–t curve and response time of the photodetector. Reprinted with permission from ref. [75]. Copyright 2018 American Chemical Society.

Du et al. developed a phototransistor based on CsPbI<sub>3</sub> nanotubes, which can be stable for more than two months under air conditions. The schematic diagram was shown in Figure 27a. The phototransistor exhibited an excellent performance with an EQE, detectivity, photoresponsivity and response time of  $5.65 \times 10^5\%$ ,  $9.99 \times 10^{13}$  Jones,  $1.84 \times 10^3$  A W<sup>-1</sup> and 3.78 ms/359 ms, respectively (Figure 27b–d). It is comparable to the best of all inorganic perovskite photodetectors, which is mainly attributed to the enhanced light absorption resulting from the light trapping effect within the tube cavity [76].

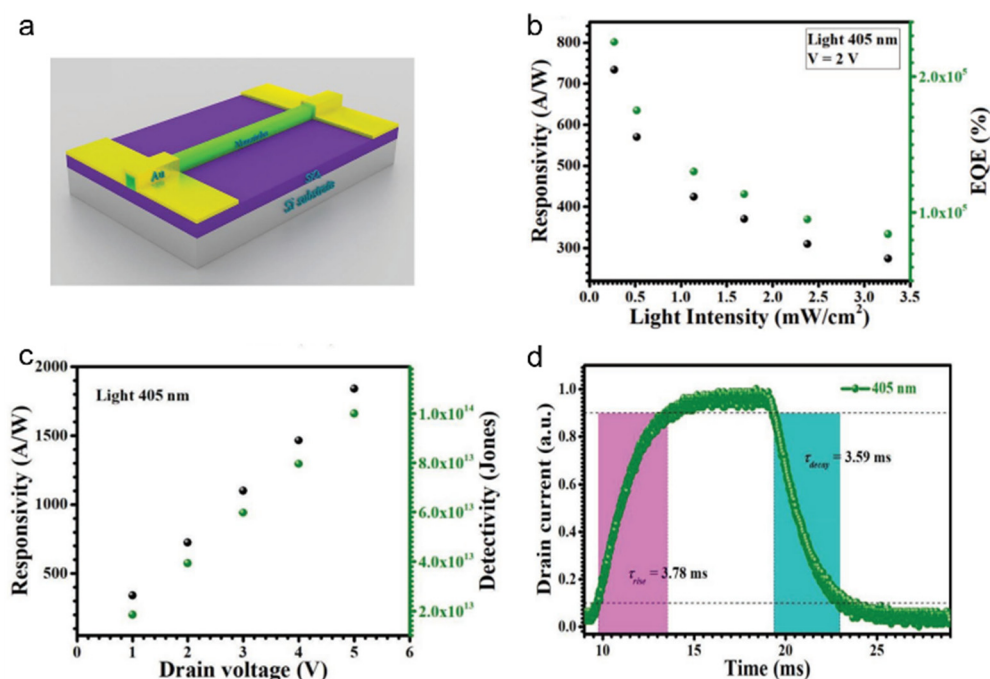


**Figure 27.** (a) The schematic diagram for the phototransistor based on CsPbI<sub>3</sub> nanotubes. (b) Responsivity and EQE vs. incident intensity. (c) Responsivity and Detectivity vs. drain voltage. (d) Response time of the device. Reprinted with permission from ref. [76]. Copyright 2019 Wiley-VCH.

### 2.2.3. Phototransistor Based on Other Nanostructured Perovskites

Kwak et al. [77] constructed a graphene/CsPbBr<sub>3-x</sub>I<sub>x</sub> NCs-based photodetector with high performance. Figure 28a illustrated the schematic of the hybrid photodetector. A responsivity as high as  $8.2 \times 10^8$  A W<sup>-1</sup> and detectivity of  $2.4 \times 10^{16}$  Jones were achieved (Figure 28b). The high performance of the phototransistor based on graphene/CsPbBr<sub>3-x</sub>I<sub>x</sub> NCs can be attributed to the fast carrier transport of graphene and strong light absorption of perovskite NCs. The photocurrent increased obviously with the increasing of incident power and showed a good on/off switching behavior (Figure 28c). The rise and decay time as shown in Figure 28d were calculated to be 0.81 s and 3.65 s, respectively.

Surendran et al. [78] demonstrated another graphene/CsPbBr<sub>x</sub>I<sub>3-x</sub> NCs-based phototransistor. Figure 29a shows the schematic diagram of the hybrid phototransistor. The PL peak and absorption edge can be redshifted to 650 nm (Figure 29b). The obviously decreased PL lifetime of hybrid structure (Figure 29c) indicates that massive charge extracted from perovskite layer and injected into graphene, and thus improving the photodetector performance (Figure 29d). The responsivity of  $1.12 \times 10^5$  A/W and the detectivity of  $1.17 \times 10^{11}$  Jones were achieved in this device (Figure 29e). The rise and decay times were 273.6 ms and 2.26 s, respectively, with excellent reproducibility (Figure 29f). Meanwhile, a large photoconductive gain of  $9.32 \times 10^{10}$  further demonstrated the potential for detecting extremely low power light. The device exhibits a significant improvement in stability with the photocurrent retention of ~82% after 37 h.

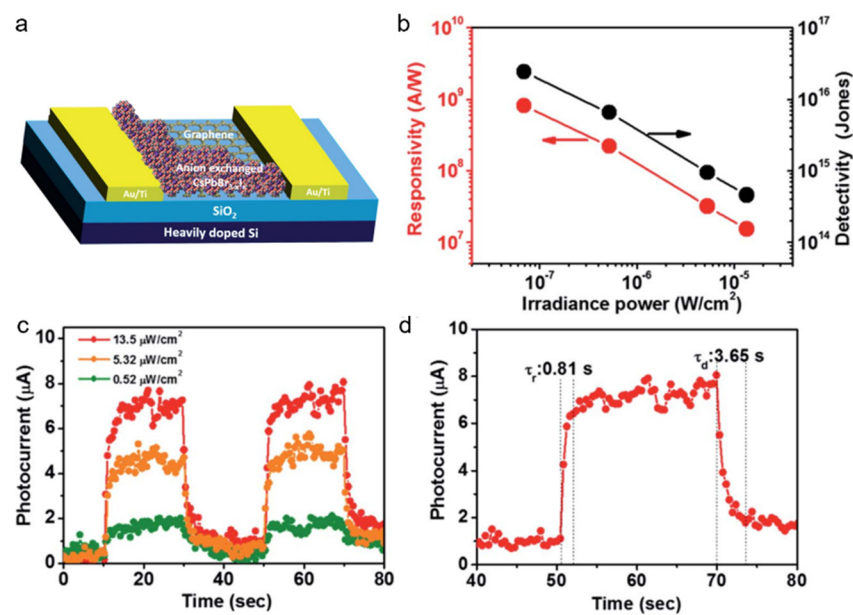


**Figure 28.** (a) Schematic of graphene/CsPbBr<sub>3-x</sub>I<sub>x</sub> NCs-based photodetector. (b) Responsivity and detectivity of the phototransistor. (c) I–t curve under different incident power. (d) Response time of the photodetector. Reprinted with permission from ref. [77]. Copyright 2015 Wiley-VCH.

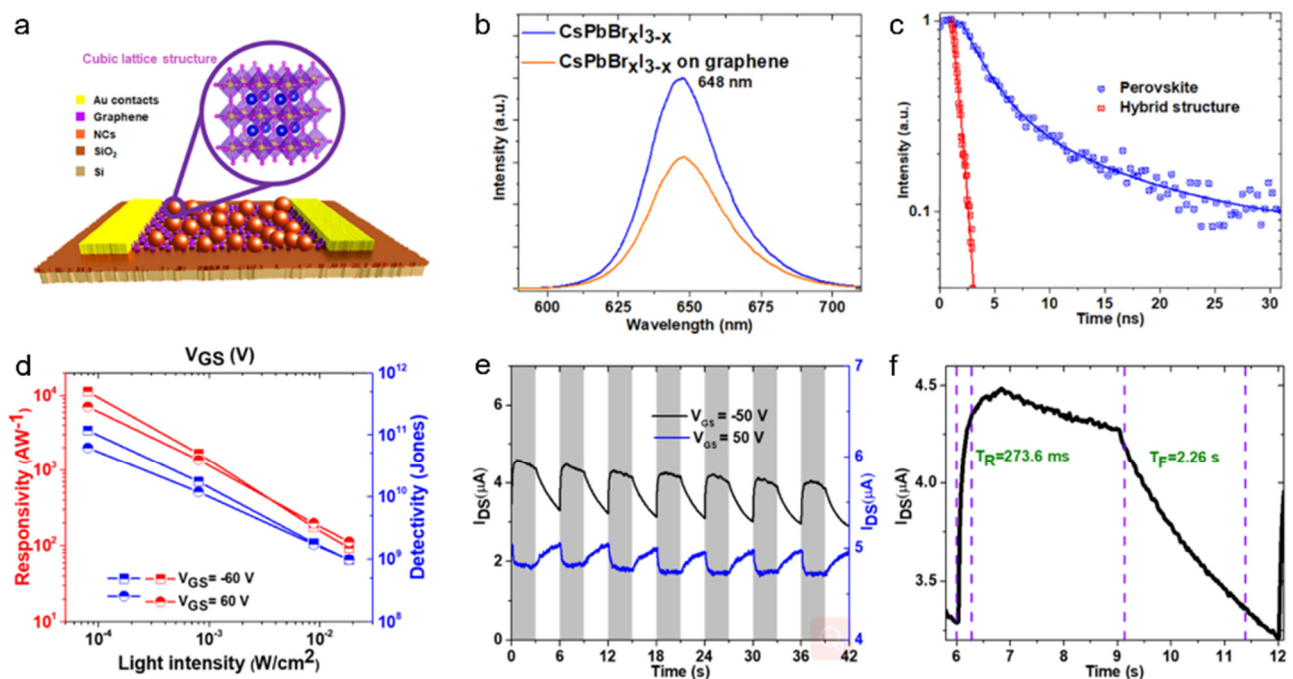


**Figure 29.** (a) Schematic diagram of the hybrid phototransistor, inset: the crystal structure of CsPbBr<sub>x</sub>I<sub>3-x</sub> NCs. (b) PL spectra of the hybrid structure. (c) A decrease of time-resolved PL in hybrid structure. (d) Responsivity and detectivity as a function of incident power. (e) I–t curve under different gate biases. (f) Response time of the phototransistor. Reprinted with permission from ref. [78]. Copyright 2019 Wiley-VCH.

Wu et al. [44] fabricated a phototransistor based on CsPbI<sub>3-x</sub>Br<sub>x</sub> quantum dots (QDs)/monolayer MoS<sub>2</sub> heterostructure with high-performance and low-cost. The schematic diagram of the phototransistor was shown in Figure 30a. The TEM image shown in Figure 30a inset demonstrated a cubic shape of the CsPbI<sub>3-x</sub>Br<sub>x</sub> quantum dots. The linear and symmetric I<sub>D</sub>–V<sub>D</sub> curves indicate a Schottky barriers at the contact interface. As shown in Figure 30b,c, the on/off ratio exceeds 10<sup>4</sup>, the photoresponsivity reach up to

$7.7 \times 10^4 \text{ A W}^{-1}$ , the specific detectivity of  $5.6 \times 10^{11} \text{ Jones}$  and an ultrahigh EQE over  $10^7\%$ . It should be noted that both R and  $D^*$  decreased exponentially with increasing incident power because of high recombination and scattering. Stable and reproducible showed a good on/off photoswitching characteristic (Figure 30d). The rise and decay times were 0.59 s and 0.32 s, respectively (Figure 30e).

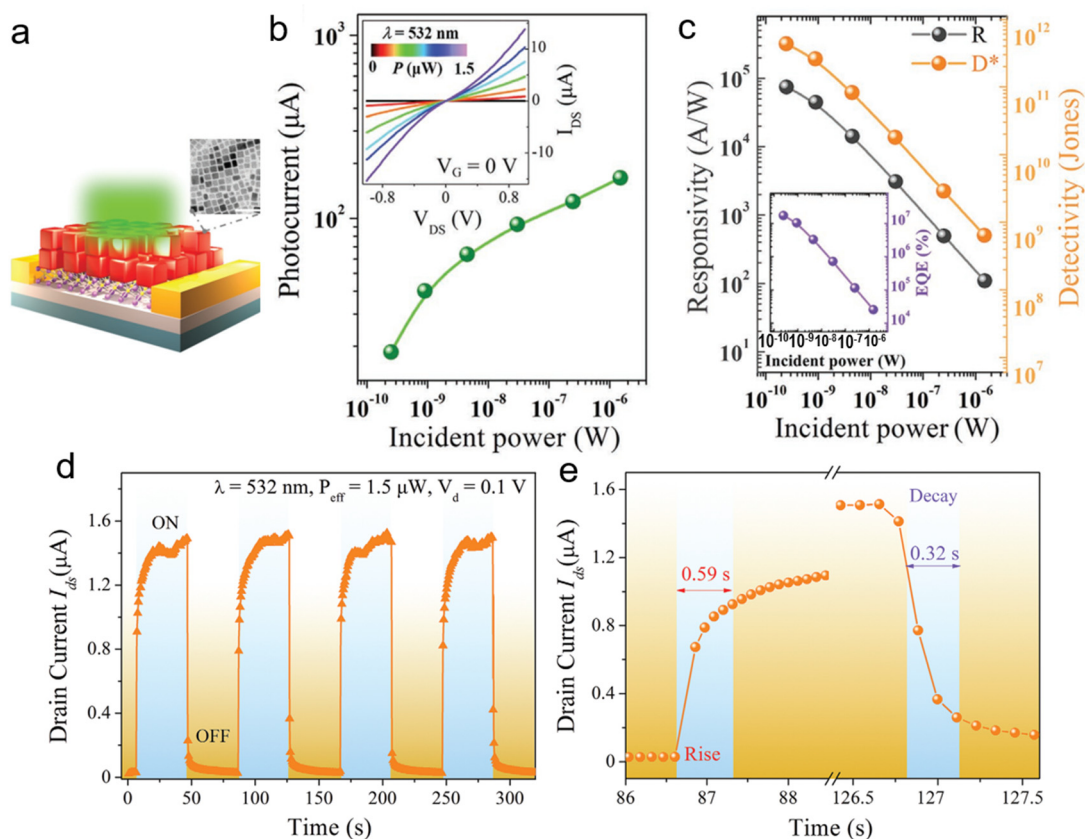


**Figure 30.** (a) Schematic of phototransistor based on CsPbI<sub>3-x</sub>Br<sub>x</sub> quantum dots/monolayer MoS<sub>2</sub> heterostructure, inset: TEM image of the CsPbI<sub>3-x</sub>Br<sub>x</sub> quantum dots. (b) Photocurrent of the phototransistor. The inset shows the I<sub>D</sub>–V<sub>D</sub> curves under different incident powers. (c) Photoresponsivity and specific detectivity of the phototransistor, inset: the EQE as a function of incident power. (d) I–t curve demonstrated a stable and reproducible photoswitch. (e) Response time of the device. Reprinted with permission from ref. [44]. Copyright 2018 Wiley-VCH.

Zou et al. [79] report a phototransistor based on CsPbI<sub>3</sub> QD/DPP-DTT heterojunction. The DPP-DTT polymer with narrow bandgap and high carrier mobility was chosen to improve the detection range and performance. The schematic was shown in Figure 31a. Figure 31b showed the intersecting surface. The phototransistor exhibits broadband detection from 350 to 940 nm by combining UV–vis absorption of CsPbI<sub>3</sub> QDs and NIR absorption of DPPDTT. A high responsivity of  $110 \text{ A W}^{-1}$  (Figure 31c) and a specific detectivity of  $2.9 \times 10^{13} \text{ Jones}$  (Figure 31d) were achieved due to the heterojunction strategy and gate modulation. The on/off ratio of  $6 \times 10^3$  (Figure 31e) indicated good photoswitching characteristics. In addition, the responsivity can be maintained 80% after one month demonstrated an excellent stability of the device.

### 2.3. Photodiode Based on Nanostructured Perovskites

Since most of the photodiode is based on thin film that is constructed by nanostructured perovskites, this part is not divided into different dimensions here. Easy to combine with other materials makes polycrystalline film a perfect choice for making photodiodes. The first perovskite photodiode using polycrystalline film as the active layer was reported by Yang et al. The device with the structure of PEDOT: PSS/MAPbI<sub>3-x</sub>Cl<sub>x</sub>/



PCBM/Al was adopted. PEDOT: PSS served as hole-transporting layer (HTL), PCBM as electron-transporting layer (ETL), and water/alcohol-soluble conjugated polymer serve as hole blocking layer. 2,9-dimethyl-4,7-diphenyl-1,10-phenanthroline (BCP) and poly[(9,9-bis(3'-(N,N-dimethylamino)propyl)-2,7-fluorene)-alt-2,7-(9,9-dioctylfluorene)] (PFN) were added to reduce the dark current density under reverse bias (Figure 32a,b). The photodetectors exhibit a high detectivity, a fast photoresponse and a linear dynamic range. (Figure 32c,d) [80] The performance is even better than commercial Si-based photodetectors. The HTL was replaced with cross-linkable N4,N4-Bis(4-(6-([3-ethyloxetan-3-yl]methoxy)hexyl)phenyl)-N4,N4-diphenylbiphenyl-4,4-diamine (OTPD) layer to reduce the dark current (Figure 32e,f). Meanwhile, PCBM/C60 double layer was employed as the hole blocking layer and C60 can passivate most of the charge traps. As a result, the dark current was suppressed to  $9.1 \times 10^{-9} \text{ A cm}^{-2}$  at  $-2 \text{ V}$ , which was much lower than the former detector using PEDOT: PSS as HTL. In addition, as shown in Figure 32g,h, the photodetector exhibits an ultrahigh detectivity of  $7.4 \times 10^{12}$  Jones, a large LDR of 94 dB and fast response time (120 ns) [81].

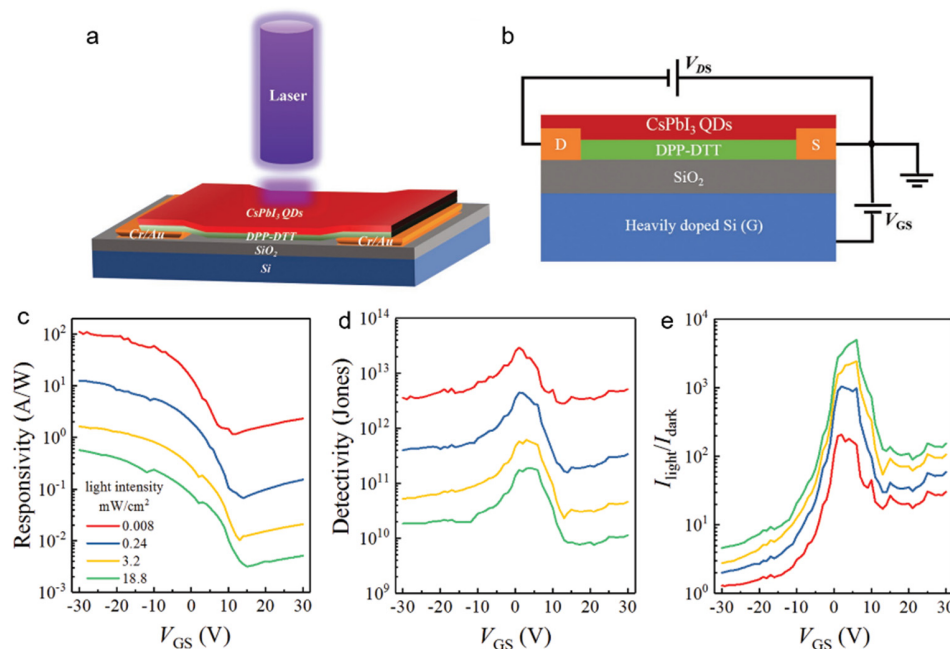


**Figure 31.** (a) The schematic of the phototransistor based on CsPbI<sub>3</sub> QD/DPP-DTT heterojunction. (b) The intersecting surface of the device. Gate-dependent (c) responsivity, (d) specific detectivity, and (e) light–dark current ratios as a function of incident power. Reprinted with permission from ref. [79]. Copyright 2018 Wiley-VCH.

Lin et al. also chose a thick PCBM/C60 interlayer as hole blocking layer to coat the perovskite homojunction and the dark current was reduced to  $5 \times 10^{-10} \text{ A cm}^{-2}$  under  $-0.5 \text{ V}$  [82]. Meanwhile, as a low shunt capacitor, the interlayer plays a key role in improving the diode temporal response. The interlayer also provides electro-optical control of the spectral response. Sutherland et al. fabricate a photodiode with a structure of Au/Spiro/MAPbI<sub>3</sub>/TiO<sub>2</sub>/FTO [83]. Addition of Al<sub>2</sub>O<sub>3</sub> and PCBM layer between TiO<sub>2</sub> and MAPbI<sub>3</sub> can effectively reduce the dark current and improve the responsivity, which should be consistent with the posited passivation of charge-trapping recombination centers at the interface (Figure 33a,b). High sensitivity throughout the visible and into the near-infrared region. As shown in Figure 33c,d, both the peak responsivity ( $0.395 \text{ A W}^{-1}$ ) and specific detectivity ( $10^{12}$  Jones) can be comparable to those of commercial silicon photodetectors [84,85]. Furthermore, the photodetector exhibits bias-independent responsivity and stable photocurrent after the detection of one billion laser pulses. These parameters indicate that perovskite materials have great potential in high-performance photode-

tectors. Dong et al. fabricated a photodiode with a structure of Ag/MoO<sub>3</sub>/4,4'-bis[(p-trichlorosilylpropylphenyl)phenylamino]-biphenyl(TPD-Si<sub>2</sub>)/MAPbI<sub>3</sub>. TPD-Si<sub>2</sub> serves as the blocking layer. MoO<sub>3</sub> is used for anode work function modification. PCBM/C60 passivation layers were cancelled to reserve surface trap states (Figure 33e,f). The large gain, which results from the hole traps caused by large concentration of Pb<sup>2+</sup> cations in the perovskite film surface, makes the as-fabricated devices work as photoconductor rather than photodiode under illumination. The photodetector exhibits a broadband response ranging from the UV to the NIR, very high responsivity of 242 A W<sup>-1</sup>, a short response time and an excellent LDR of 85 dB (Figure 33g,h) [86].

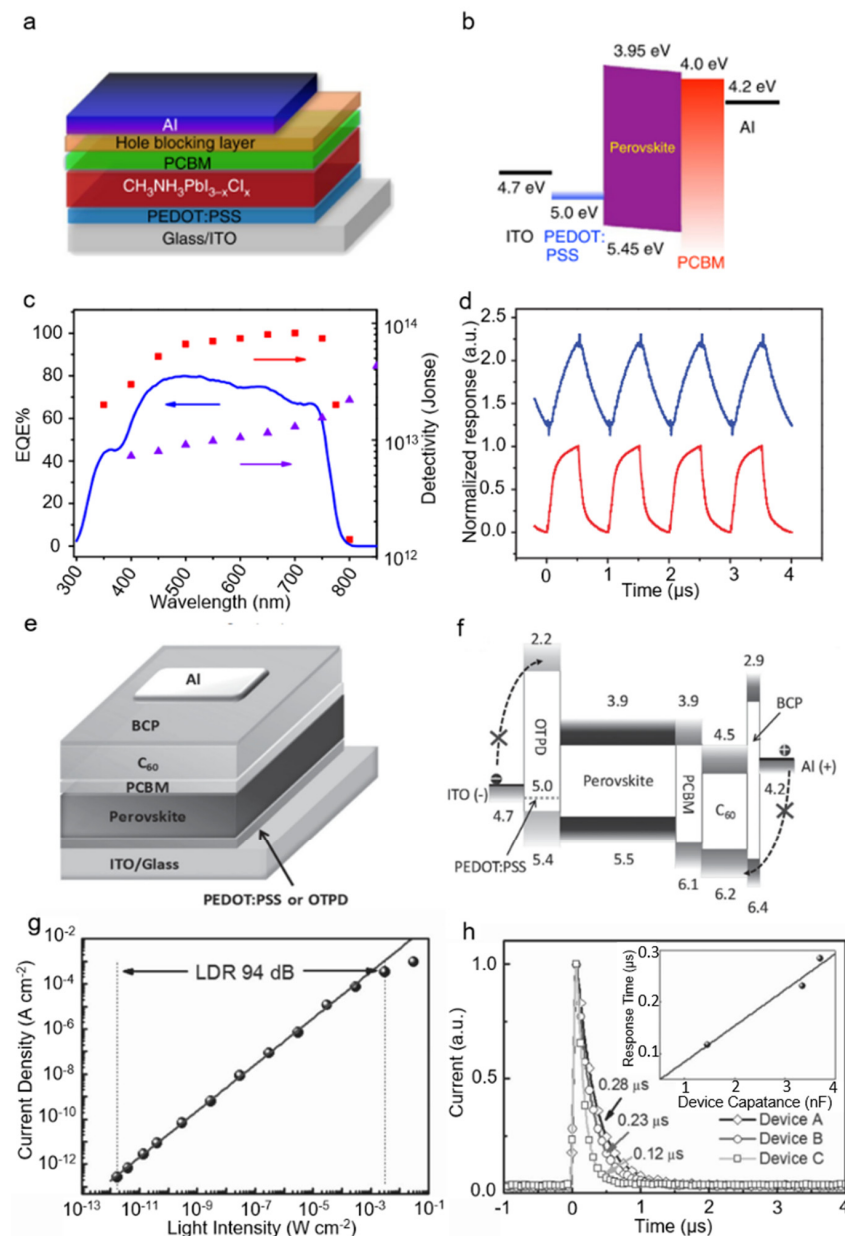


**Figure 32.** (a) The schematic of the photovoltaic device. (b) Energy diagram of the device. (c) EQE and detectivity of the photodetector at different wavelength. (d) Transient photocurrent response of the photodetector at a pulse frequency of 1 MHz with a device area of 0.1 cm<sup>2</sup> (blue line) and 0.01 cm<sup>2</sup> (red line), respectively. Copyright 2014, Nature Publishing Group [80] (e) The schematic of perovskite photodetectors. (f) The energy diagram of the perovskite photodetectors. (g) Dynamic response of the photodetector. (h) The short photoresponse time of the device. Reprinted with permission from ref. [81]. Copyright 2015 Wiley-VCH.

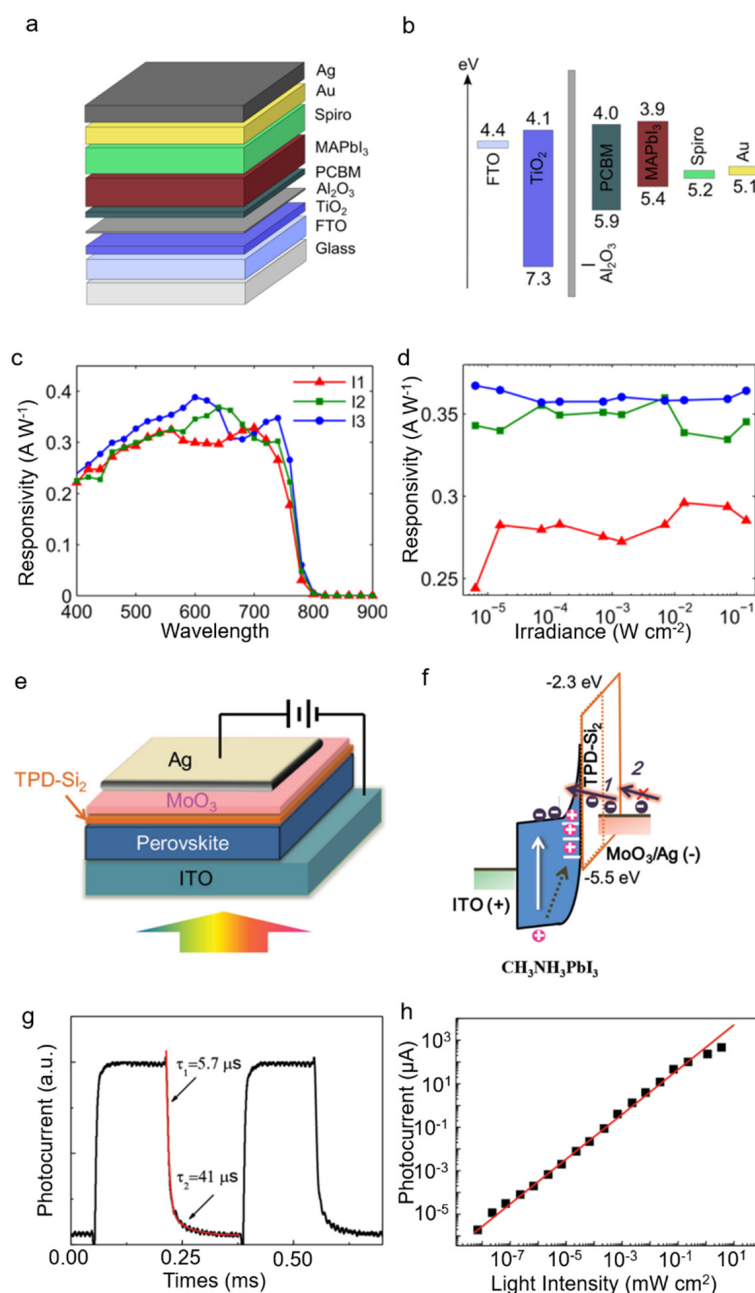


**Figure 33.** (a) The schematic of the photovoltaic device. (b) Energy diagram of the device. (c) Broadband response spectra of the device. (d) Responsivity versus incident light with different intensities. Copyright 2015, American Chemical Society [83]. (e) The schematic of the MoO<sub>3</sub>-MAPbI<sub>3</sub> photodetector. (f) Energy diagram of the photodetector. (g) Transient photocurrent of the MAPbI<sub>3</sub> photodetector. (h) Dynamic response of the photodetector. Reprinted with permission from ref. [86]. Copyright 2015 Wiley-VCH.

In Table 2, we summarize some key parameters of the photoconductors based on nanostructured perovskites. It seems that 1D perovskite-based photodetectors are much more studied and often perform better than 2D perovskite-based photodetectors. This may be due to the relatively better crystal quality of 1D perovskites and better ohmic contact between 1D perovskites and electrodes.

Table 2. Key characteristics of nanostructured perovskites-based photodetectors.

Device	Dimension	Perovskite	R	D	EQE	On/Off Ratio	Gain	LDR	Rise/Decay Time	Ref.	
Photoconductor	2D	CsPbBr <sub>3</sub>	0.25		53%				19 μs/25 μs	[43]	
		MAPbI <sub>3</sub>				1210				[53]	
		CsPbBr <sub>3</sub> /CNTs	31.1		7488%				16 μs/0.38 ms	[55]	
	1D	MAPbI <sub>3</sub>	13.57	5.25 × 10 <sup>12</sup>							[56]
		MAPbI <sub>3</sub>	0.04	0.6 × 10 <sup>12</sup>			0.84 × 10 <sup>4</sup>			178 μs/173 μs	[57]
		MAPbBr <sub>3</sub>					61.9			0.12 s/0.086 s	[58]
		MAPb(I <sub>1-x</sub> Br <sub>x</sub> ) <sub>3</sub>	1.25 × 10 <sup>4</sup>	1.73 × 10 <sup>11</sup>				36,800	150		[59]
		MAPb(I/Br) <sub>3</sub>	10 <sup>3</sup>				2000			0.68 s/0.66 s	[60]
		MAPbI <sub>3</sub>	0.45	2 × 10 <sup>13</sup>			4000			<0.1 ms	[61]
		MAPbI <sub>3</sub>	1.2	2.39 × 10 <sup>12</sup>			160				[62]
		CsPbI <sub>3</sub>	1294	2.6 × 10 <sup>14</sup>						0.85 ms/0.78 ms	[42]
		CsSnI <sub>3</sub>	0.054	3.85 × 10 <sup>5</sup>						83.8 ms/243.4 ms	[63]
		CsCu <sub>2</sub> I <sub>3</sub>	32.3	1.89 × 10 <sup>12</sup>				2.6 × 10 <sup>3</sup>		6.94 μs/214 μs	[64]
	others	CsPbBr <sub>3</sub>	0.0209				1.6 × 10 <sup>5</sup>			0.2 ms/1.3 s	[65]
		CsPbX <sub>3</sub>					10 <sup>5</sup>			24 ms/29 ms	[52]
GQDs/CsPbBr <sub>3</sub>		0.24	2.5 × 10 <sup>12</sup>	57%	7.2 × 10 <sup>4</sup>				1.16 ms (Decay)	[66]	
Phototransistor	2D	MAPbX <sub>3</sub>	22			10 <sup>12</sup>			20 ms/40 ms	[67]	
		CsPbBr <sub>3</sub>							17.8 ms/(14.7 ms/15.2 ms)	[68]	
	1D	MAPbI <sub>3</sub>					4.02 × 10 <sup>3</sup>			0.35 ms/0.25 ms	[69]
		MAPbI <sub>3</sub>	0.3					0.25		0.2 ms/0.25 ms	[70]
		MAPbI <sub>3</sub>	0.11								[71]
		MAPbI <sub>3</sub>	2.6 × 10 <sup>6</sup>							55 s/75 s	[72]
		C8BTBT/CsPbI <sub>3</sub>	4.3 × 10 <sup>3</sup>				2.2 × 10 <sup>6</sup>				[73]
		CsPbX <sub>3</sub>	4489	7.9 × 10 <sup>12</sup>						<50 ms	[74]
		CsPbI <sub>3</sub>	2.92 × 10 <sup>3</sup>	5.17 × 10 <sup>13</sup>	0.6 × 10 <sup>6</sup> %					50ms	[75]
	CsPbI <sub>3</sub>	1.84 × 10 <sup>3</sup>	9.9 × 10 <sup>13</sup>	5.65 × 10 <sup>5</sup> %					3.78 ms/539 ms	[76]	
	others	Graphene/CsPbBr <sub>3-x</sub> I <sub>x</sub>	8.2 × 10 <sup>8</sup>	2.4 × 10 <sup>16</sup>						0.81 s/3.65 s	[77]
		Graphene/CsPbBr <sub>x</sub> I <sub>3-x</sub>	1.12 × 10 <sup>5</sup>	1.17 × 10 <sup>11</sup>				9.32 × 10 <sup>10</sup>		273.6 ms/2.26 s	[78]
CsPbI <sub>3-x</sub> Br <sub>x</sub>		7.7 × 10 <sup>4</sup>	5.6 × 10 <sup>11</sup>	107%					0.59 s/0.32 s	[44]	
CsPbI <sub>3</sub> /DPP-DTT		110	2.9 × 10 <sup>13</sup>			6 × 10 <sup>3</sup>				[79]	

### 3. Conclusions and Outlook

In summary, the research advancements of nanostructured perovskite-based photodetectors are reviewed. The performances of the detectors are influenced by the type of devices as well as the structures of nanostructured perovskites with different morphology. As a whole, photodetectors based on nanostructure perovskites perform well due to long carrier lifetime, great carrier mobility, and low carrier recombination result from few grain boundary and lower trap state density. Our conclusion is that nanostructured perovskites have great potential to be applied in low-voltage, low-cost, fast-response, high-detectivity, and ultra-highly integrated optoelectronic devices.

Despite great progress has been made on the perovskite photodetectors, there are still many challenges. First, both the photoconductors and phototransistors only achieve part of photodetection parameters enhancement. However, an ideal photodetector should improve performance including high responsivity, large detectivity, fast speed, etc. Second, perovskites easily degrade in air with the presence of oxygen and moisture. Thus, the instability of perovskite impedes the commercial use of the device. It is of great significance to improve the perovskite with new protection strategies though the heterojunction structures exhibit relatively better stability. In addition, some literatures only reported the best performance of the device, but ignored the average performance of the device, which would lead to a misleading effect on the industrialization direction, and also show that the authors have no confidence in the stability of the device. Finally, the toxicity of perovskite has cast a shadow over its application because of the use of lead in widely studied materials, such as MAPbI<sub>3</sub>, and CsPbBr<sub>3</sub>. Therefore, more efforts should be made to prepare environmental perovskite materials with non-toxic elements instead of Pb.

**Funding:** This work is funded by the National Natural Science Foundation of China (Grant No. 51802215), and the Foundation (No. ZZ20190206 and No. ZR20190107) of State Key Laboratory of Biobased Material and Green Papermaking, Qilu University of Technology, Shandong Academy of Sciences. Y.D. acknowledges the China Postdoctoral Science Foundation (Grant No. 2017M621067 and 2018T110197).

**Conflicts of Interest:** There are no conflicts to declare.

### References

1. Xu, Z.; Zhang, Y.; Wang, Z. ZnO-based photodetector: From photon detector to pyro-phototronic effect enhanced detector. *J. Phys. D Appl. Phys.* **2019**, *52*, 223001. [[CrossRef](#)]
2. Li, D.; Jiang, K.; Sun, X.; Guo, C. AlGaIn photonics: Recent advances in materials and ultraviolet devices. *Adv. Opt. Photonics* **2018**, *10*, 43–110. [[CrossRef](#)]
3. Oh, S.; Kim, C.-K.; Kim, J. High responsivity  $\beta$ -Ga<sub>2</sub>O<sub>3</sub> metal–semiconductor–metal solar-blind photodetectors with ultraviolet transparent graphene electrodes. *ACS Photonics* **2017**, *5*, 1123–1128. [[CrossRef](#)]
4. Qi, J.; Qiao, W.; Zhou, X.; Yang, D.; Zhang, J.; Ma, D.; Wang, Z.Y. High-Detectivity All-Polymer Photodetectors with Spectral Response from 300 to 1100 nm. *Macromol. Chem. Phys.* **2016**, *217*, 1683–1689. [[CrossRef](#)]
5. Luo, L.-B.; Yang, X.-B.; Liang, F.-X.; Jie, J.-S.; Li, Q.; Zhu, Z.-F.; Wu, C.-Y.; Yu, Y.-Q.; Wang, L. Transparent and flexible selenium nanobelt-based visible light photodetector. *CrystEngComm* **2012**, *14*, 1942–1947. [[CrossRef](#)]
6. Qiu, X.; Wang, Z.; Hou, X.; Yu, X.; Yang, D. Visible-blind short-wavelength infrared photodetector with high responsivity based on hyperdoped silicon. *Photonics Res.* **2019**, *7*, 351–358. [[CrossRef](#)]
7. Yu, P.; Hu, K.; Chen, H.; Zheng, L.; Fang, X. Novel p–p Heterojunctions Self-Powered Broadband Photodetectors with Ultrafast Speed and High Responsivity. *Adv. Funct. Mater.* **2017**, *27*, 1703166. [[CrossRef](#)]
8. Gong, F.; Fang, H.; Wang, P.; Su, M.; Li, Q.; Ho, J.C.; Chen, X.; Lu, W.; Liao, L.; Wang, J. Visible to near-infrared photodetectors based on MoS<sub>2</sub> vertical Schottky junctions. *Nanotechnology* **2017**, *28*, 484002. [[CrossRef](#)] [[PubMed](#)]
9. Wang, L.; Jie, J.; Shao, Z.; Zhang, Q.; Zhang, X.; Wang, Y.; Sun, Z.; Lee, S.T. MoS<sub>2</sub>/Si heterojunction with vertically standing layered structure for ultrafast, high-detectivity, self-driven visible-near infrared photodetectors. *Adv. Funct. Mater.* **2015**, *25*, 2910–2919. [[CrossRef](#)]
10. Rogalski, A.; Antoszewski, J.; Faraone, L. Third-generation infrared photodetector arrays. *J. Appl. Phys.* **2009**, *105*, 4. [[CrossRef](#)]
11. Meledin, D.V.; Marrone, D.P.; Tong, C.-Y.; Gibson, H.; Blundell, R.; Paine, S.N.; Papa, D.C.; Smith, M.; Hunter, T.R.; Battat, J. A 1-THz superconducting hot-electron-bolometer receiver for astronomical observations. *IEEE Trans. Microw. Theory Tech.* **2004**, *52*, 2338–2343. [[CrossRef](#)]
12. Tong, C.-Y.; Meledin, D.V.; Marrone, D.P.; Paine, S.N.; Gibson, H.; Blundell, R. Near field vector beam measurements at 1 THz. *IEEE Microw. Wirel. Compon. Lett.* **2003**, *13*, 235–237. [[CrossRef](#)]

13. Mittleman, D.M. Twenty years of terahertz imaging. *Opt. Express* **2018**, *26*, 9417–9431. [[CrossRef](#)]
14. Zhang, H.; Zhang, X.; Liu, C.; Lee, S.-T.; Jie, J. High-responsivity, high-detectivity, ultrafast topological insulator Bi<sub>2</sub>Se<sub>3</sub>/silicon heterostructure broadband photodetectors. *ACS Nano* **2016**, *10*, 5113–5122. [[CrossRef](#)] [[PubMed](#)]
15. Xie, C.; Nie, B.; Zeng, L.; Liang, F.-X.; Wang, M.-Z.; Luo, L.; Feng, M.; Yu, Y.; Wu, C.-Y.; Wu, Y. Core-shell heterojunction of silicon nanowire arrays and carbon quantum dots for photovoltaic devices and self-driven photodetectors. *ACS Nano* **2014**, *8*, 4015–4022. [[CrossRef](#)]
16. Zhang, A.; Kim, H.; Cheng, J.; Lo, Y.-H. Ultrahigh responsivity visible and infrared detection using silicon nanowire phototransistors. *Nano Lett.* **2010**, *10*, 2117–2120. [[CrossRef](#)]
17. Barone, P.W.; Baik, S.; Heller, D.A.; Strano, M.S. Near-infrared optical sensors based on single-walled carbon nanotubes. *Nat. Mater.* **2005**, *4*, 86–92. [[CrossRef](#)] [[PubMed](#)]
18. Arnold, M.S.; Zimmerman, J.D.; Renshaw, C.K.; Xu, X.; Lunt, R.R.; Austin, C.M.; Forrest, S.R. Broad spectral response using carbon nanotube/organic semiconductor/C60 photodetectors. *Nano Lett.* **2009**, *9*, 3354–3358. [[CrossRef](#)] [[PubMed](#)]
19. Kind, H.; Yan, H.; Messer, B.; Law, M.; Yang, P. Nanowire ultraviolet photodetectors and optical switches. *Adv. Mater.* **2002**, *14*, 158–160. [[CrossRef](#)]
20. Jin, Y.; Wang, J.; Sun, B.; Blakesley, J.C.; Greenham, N.C. Solution-processed ultraviolet photodetectors based on colloidal ZnO nanoparticles. *Nano Lett.* **2008**, *8*, 1649–1653. [[CrossRef](#)] [[PubMed](#)]
21. Baeg, K.J.; Binda, M.; Natali, D.; Caironi, M.; Noh, Y.Y. Organic light detectors: Photodiodes and phototransistors. *Adv. Mater.* **2013**, *25*, 4267–4295. [[CrossRef](#)] [[PubMed](#)]
22. Herman, M.A.; Sitter, H. *Molecular Beam Epitaxy: Fundamentals and Current Status*; Springer: Berlin/Heidelberg, Germany, 2012; Volume 7.
23. Bao, C.; Zhu, W.; Yang, J.; Li, F.; Gu, S.; Wang, Y.; Yu, T.; Zhu, J.; Zhou, Y.; Zou, Z. Highly flexible self-powered organolead trihalide perovskite photodetectors with gold nanowire networks as transparent electrodes. *ACS Appl. Mater. Interfaces* **2016**, *8*, 23868–23875. [[CrossRef](#)]
24. Lin, Q.; Armin, A.; Burn, P.L.; Meredith, P. Filterless narrowband visible photodetectors. *Nat. Photonics* **2015**, *9*, 687–694. [[CrossRef](#)]
25. Maculan, G.; Sheikh, A.D.; Abdelhady, A.L.; Saidaminov, M.I.; Haque, M.A.; Murali, B.; Alarousu, E.; Mohammed, O.F.; Wu, T.; Bakr, O.M. CH<sub>3</sub>NH<sub>3</sub>PbCl<sub>3</sub> single crystals: Inverse temperature crystallization and visible-blind UV-photodetector. *J. Phys. Chem. Lett.* **2015**, *6*, 3781–3786. [[CrossRef](#)] [[PubMed](#)]
26. Xing, G.; Mathews, N.; Sun, S.; Lim, S.S.; Lam, Y.M.; Grätzel, M.; Mhaisalkar, S.; Sum, T.C. Long-range balanced electron-and hole-transport lengths in organic-inorganic CH<sub>3</sub>NH<sub>3</sub>PbI<sub>3</sub>. *Science* **2013**, *342*, 344–347. [[CrossRef](#)]
27. Bekenstein, Y.; Koscher, B.A.; Eaton, S.W.; Yang, P.; Alivisatos, A.P. Highly Luminescent Colloidal Nanoplates of Perovskite Cesium Lead Halide and Their Oriented Assemblies. *J. Am. Chem. Soc.* **2015**, *137*, 16008–16011. [[CrossRef](#)] [[PubMed](#)]
28. Tong, Y.L.; Zhang, Y.W.; Ma, K.; Cheng, R.; Wang, F.; Chen, S. One-Step Synthesis of FA-Directing FAPbBr<sub>3</sub> Perovskite Nanocrystals toward High-Performance Display. *ACS Appl. Mater. Interfaces* **2018**, *10*, 31603–31609. [[CrossRef](#)]
29. Takahashi, Y.; Hasegawa, H.; Takahashi, Y.; Inabe, T. Hall mobility in tin iodide perovskite CH<sub>3</sub>NH<sub>3</sub>SnI<sub>3</sub>: Evidence for a doped semiconductor. *J. Solid State Chem.* **2013**, *205*, 39–43. [[CrossRef](#)]
30. Yin, W.J.; Shi, T.; Yan, Y. Unique properties of halide perovskites as possible origins of the superior solar cell performance. *Adv. Mater.* **2014**, *26*, 4653–4658. [[CrossRef](#)]
31. Hu, X.; Zhang, X.; Liang, L.; Bao, J.; Li, S.; Yang, W.; Xie, Y. High-Performance Flexible Broadband Photodetector Based on Organolead Halide Perovskite. *Adv. Funct. Mater.* **2014**, *24*, 7373–7380. [[CrossRef](#)]
32. Saidaminov, M.I.; Adinolfi, V.; Comin, R.; Abdelhady, A.L.; Peng, W.; Dursun, I.; Yuan, M.; Hoogland, S.; Sargent, E.H.; Bakr, O.M. Planar-integrated single-crystalline perovskite photodetectors. *Nature Commun.* **2015**, *6*, 1–7. [[CrossRef](#)] [[PubMed](#)]
33. Fang, Y.; Dong, Q.; Shao, Y.; Yuan, Y.; Huang, J. Highly narrowband perovskite single-crystal photodetectors enabled by surface-charge recombination. *Nat. Photonics* **2015**, *9*, 679–686. [[CrossRef](#)]
34. Han, Q.; Bae, S.H.; Sun, P.; Hsieh, Y.T.; Yang, Y.; Rim, Y.S.; Zhao, H.; Chen, Q.; Shi, W.; Li, G. Single crystal formamidinium lead iodide (FAPbI<sub>3</sub>): Insight into the structural, optical, and electrical properties. *Adv. Mater.* **2016**, *28*, 2253–2258. [[CrossRef](#)] [[PubMed](#)]
35. Liu, X.; Gu, L.; Zhang, Q.; Wu, J.; Long, Y.; Fan, Z. All-printable band-edge modulated ZnO nanowire photodetectors with ultra-high detectivity. *Nat. Commun.* **2014**, *5*, 1–9. [[CrossRef](#)]
36. Wu, X.; Trinh, M.T.; Niesner, D.; Zhu, H.; Norman, Z.; Owen, J.S.; Yaffe, O.; Kudisch, B.J.; Zhu, X.-Y. Trap states in lead iodide perovskites. *J. Am. Chem. Soc.* **2015**, *137*, 2089–2096. [[CrossRef](#)]
37. De Quilletes, D.W.; Vorpahl, S.M.; Stranks, S.D.; Nagaoka, H.; Eperon, G.E.; Ziffer, M.E.; Snaith, H.J.; Ginger, D.S. Impact of microstructure on local carrier lifetime in perovskite solar cells. *Science* **2015**, *348*, 683–686. [[CrossRef](#)]
38. Soci, C.; Zhang, A.; Xiang, B.; Dayeh, S.A.; Aplin, D.; Park, J.; Bao, X.; Lo, Y.-H.; Wang, D. ZnO nanowire UV photodetectors with high internal gain. *Nano Lett.* **2007**, *7*, 1003–1009. [[CrossRef](#)]
39. McDonald, S.A.; Konstantatos, G.; Zhang, S.; Cyr, P.W.; Klem, E.J.; Levina, L.; Sargent, E.H. Solution-processed PbS quantum dot infrared photodetectors and photovoltaics. *Nat. Mater.* **2005**, *4*, 138–142. [[CrossRef](#)]
40. Fang, X.; Bando, Y.; Liao, M.; Gautam, U.K.; Zhi, C.; Dierre, B.; Liu, B.; Zhai, T.; Sekiguchi, T.; Koide, Y. Single-crystalline ZnS nanobelts as ultraviolet-light sensors. *Adv. Mater.* **2009**, *21*, 2034–2039. [[CrossRef](#)]

41. Huang, X.; Wang, M.; Willinger, M.-G.; Shao, L.; Su, D.S.; Meng, X.-M. Assembly of three-dimensional hetero-epitaxial ZnO/ZnS core/shell nanorod and single crystalline hollow ZnS nanotube arrays. *ACS Nano* **2012**, *6*, 7333–7339. [[CrossRef](#)]
42. Chen, G.; Feng, J.; Gao, H.; Zhao, Y.; Pi, Y.; Jiang, X.; Wu, Y.; Jiang, L. Stable  $\alpha$ -CsPbI<sub>3</sub> Perovskite Nanowire Arrays with Preferential Crystallographic Orientation for Highly Sensitive Photodetectors. *Adv. Funct. Mater.* **2019**, *29*, 1808741. [[CrossRef](#)]
43. Song, J.; Xu, L.; Li, J.; Xue, J.; Dong, Y.; Li, X.; Zeng, H. Monolayer and Few-Layer All-Inorganic Perovskites as a New Family of Two-Dimensional Semiconductors for Printable Optoelectronic Devices. *Adv. Mater.* **2016**, *28*, 4861–4869. [[CrossRef](#)]
44. Wu, H.; Si, H.; Zhang, Z.; Kang, Z.; Wu, P.; Zhou, L.; Zhang, S.; Zhang, Z.; Liao, Q.; Zhang, Y. All-Inorganic Perovskite Quantum Dot-Monolayer MoS<sub>2</sub> Mixed-Dimensional van der Waals Heterostructure for Ultrasensitive Photodetector. *Adv. Sci.* **2018**, *5*, 1801219. [[CrossRef](#)] [[PubMed](#)]
45. Gu, H.; Chen, S.C.; Zheng, Q. Emerging Perovskite Materials with Different Nanostructures for Photodetectors. *Adv. Opt. Mater.* **2020**, 2001637. [[CrossRef](#)]
46. Wang, H.P.; Li, S.; Liu, X.; Shi, Z.; Fang, X.; He, J.H. Low-Dimensional Metal Halide Perovskite Photodetectors. *Adv. Mater.* **2021**, *33*, e2003309. [[CrossRef](#)]
47. Song, J.; Cui, Q.; Li, J.; Xu, J.; Wang, Y.; Xu, L.; Xue, J.; Dong, Y.; Tian, T.; Sun, H.; et al. Ultralarge All-Inorganic Perovskite Bulk Single Crystal for High-Performance Visible-Infrared Dual-Modal Photodetectors. *Adv. Opt. Mater.* **2017**, *5*, 1700157. [[CrossRef](#)]
48. Liang, F.-X.; Wang, J.-Z.; Zhang, Z.-X.; Wang, Y.-Y.; Gao, Y.; Luo, L.-B. Broadband, Ultrafast, Self-Driven Photodetector Based on Cs-Doped FAPbI<sub>3</sub> Perovskite Thin Film. *Adv. Opt. Mater.* **2017**, *5*, 1700654. [[CrossRef](#)]
49. Wang, F.; Mei, J.; Wang, Y.; Zhang, L.; Zhao, H.; Zhao, D. Fast Photoconductive Responses in Organometal Halide Perovskite Photodetectors. *ACS Appl. Mater. Interfaces* **2016**, *8*, 2840–2846. [[CrossRef](#)] [[PubMed](#)]
50. Li, Y.; Shi, Z.-F.; Li, S.; Lei, L.-Z.; Ji, H.-F.; Wu, D.; Xu, T.-T.; Tian, Y.-T.; Li, X.-J. High-performance perovskite photodetectors based on solution-processed all-inorganic CsPbBr<sub>3</sub> thin films. *J. Mater. Chem.* **2017**, *5*, 8355–8360. [[CrossRef](#)]
51. Li, F.; Ma, C.; Wang, H.; Hu, W.; Yu, W.; Sheikh, A.D.; Wu, T. Ambipolar solution-processed hybrid perovskite phototransistors. *Nat. Commun.* **2015**, *6*. [[CrossRef](#)] [[PubMed](#)]
52. Ramasamy, P.; Lim, D.-H.; Kim, B.; Lee, S.-H.; Lee, M.-S.; Lee, J.-S. All-inorganic cesium lead halide perovskite nanocrystals for photodetector applications. *Chem. Commun.* **2016**, *52*, 2067–2070. [[CrossRef](#)]
53. Qin, X.; Yao, Y.; Dong, H.; Zhen, Y.; Jiang, L.; Hu, W. Perovskite Photodetectors based on CH<sub>3</sub>NH<sub>3</sub>PbI<sub>3</sub> Single Crystals. *Chem. Asian J.* **2016**, *11*, 2675–2679. [[CrossRef](#)]
54. Xia, H.-R.; Li, J.; Sun, W.-T.; Peng, L.-M. Organohalide lead perovskite based photodetectors with much enhanced performance. *Chem. Commun.* **2014**, *50*, 13695–13697. [[CrossRef](#)] [[PubMed](#)]
55. Li, X.; Yu, D.; Chen, J.; Wang, Y.; Cao, F.; Wei, Y.; Wu, Y.; Wang, L.; Zhu, Y.; Sun, Z.; et al. Constructing Fast Carrier Tracks into Flexible Perovskite Photodetectors To Greatly Improve Responsivity. *ACS Nano* **2017**, *11*, 2015–2023. [[CrossRef](#)] [[PubMed](#)]
56. Deng, W.; Zhang, X.; Huang, L.; Xu, X.; Wang, L.; Wang, J.; Shang, Q.; Lee, S.T.; Jie, J. Aligned Single-Crystalline Perovskite Microwire Arrays for High-Performance Flexible Image Sensors with Long-Term Stability. *Adv. Mater.* **2016**, *28*, 2201–2208. [[CrossRef](#)] [[PubMed](#)]
57. Li, S.; Li, Y.; Shi, Z.; Lei, L.; Ji, H.; Wu, D.; Xu, T.; Li, X.; Du, G. Fabrication of morphology-controlled and highly-crystallized perovskite microwires for long-term stable photodetectors. *Sol. Energy Mater. Sol. Cells* **2019**, *191*, 275–282. [[CrossRef](#)]
58. Zhuo, S.; Zhang, J.; Shi, Y.; Huang, Y.; Zhang, B. Self-template-directed synthesis of porous perovskite nanowires at room temperature for high-performance visible-light photodetectors. *Angew. Chem.* **2015**, *54*, 5693–5696. [[CrossRef](#)]
59. Deng, W.; Huang, L.; Xu, X.; Zhang, X.; Jin, X.; Lee, S.T.; Jie, J. Ultrahigh-Responsivity Photodetectors from Perovskite Nanowire Arrays for Sequentially Tunable Spectral Measurement. *Nano Lett.* **2017**, *17*, 2482–2489. [[CrossRef](#)] [[PubMed](#)]
60. Tang, X.; Zu, Z.; Shao, H.; Hu, W.; Zhou, M.; Deng, M.; Chen, W.; Zang, Z.; Zhu, T.; Xue, J. All-inorganic perovskite CsPb(Br/I)<sub>3</sub> nanorods for optoelectronic application. *Nanoscale* **2016**, *8*, 15158–15161. [[CrossRef](#)]
61. Gao, L.; Zeng, K.; Guo, J.; Ge, C.; Du, J.; Zhao, Y.; Chen, C.; Deng, H.; He, Y.; Song, H.; et al. Passivated Single-Crystalline CH<sub>3</sub>NH<sub>3</sub>PbI<sub>3</sub> Nanowire Photodetector with High Detectivity and Polarization Sensitivity. *Nano Lett.* **2016**, *16*, 7446–7454. [[CrossRef](#)]
62. Liu, Y.; Li, F.; Perumal Veeramalai, C.; Chen, W.; Guo, T.; Wu, C.; Kim, T.W. Inkjet-Printed Photodetector Arrays Based on Hybrid Perovskite CH<sub>3</sub>NH<sub>3</sub>PbI<sub>3</sub> Microwires. *ACS Appl. Mater. Interfaces* **2017**, *9*, 11662–11668. [[CrossRef](#)] [[PubMed](#)]
63. Han, M.; Sun, J.; Peng, M.; Han, N.; Chen, Z.; Liu, D.; Guo, Y.; Zhao, S.; Shan, C.; Xu, T.; et al. Controllable Growth of Lead-Free All-Inorganic Perovskite Nanowire Array with Fast and Stable Near-Infrared Photodetection. *J. Phys. Chem.* **2019**, *123*, 17566–17573. [[CrossRef](#)]
64. Li, Y.; Shi, Z.; Wang, L.; Chen, Y.; Liang, W.; Wu, D.; Li, X.; Zhang, Y.; Shan, C.; Fang, X. Solution-processed one-dimensional CsCu<sub>2</sub>I<sub>3</sub> nanowires for polarization-sensitive and flexible ultraviolet photodetectors. *Mater. Horiz.* **2020**, *7*, 1613–1622. [[CrossRef](#)]
65. Dong, Y.; Gu, Y.; Zou, Y.; Song, J.; Xu, L.; Li, J.; Xue, J.; Li, X.; Zeng, H. Improving All-Inorganic Perovskite Photodetectors by Preferred Orientation and Plasmonic Effect. *Small* **2016**, *12*, 5622–5632. [[CrossRef](#)]
66. Algadi, H.; Mahata, C.; Sahoo, B.; Kim, M.; Koh, W.-G.; Lee, T. Facile method for the preparation of high-performance photodetectors with a GQDs/perovskite bilayer heterostructure. *Org. Electron.* **2020**, *76*, 105444. [[CrossRef](#)]
67. Liu, J.; Xue, Y.; Wang, Z.; Xu, Z.Q.; Zheng, C.; Weber, B.; Song, J.; Wang, Y.; Lu, Y.; Zhang, Y.; et al. Two-Dimensional CH<sub>3</sub>NH<sub>3</sub>PbI<sub>3</sub> Perovskite: Synthesis and Optoelectronic Application. *ACS Nano* **2016**, *10*, 3536–3542. [[CrossRef](#)]

68. Lv, L.; Xu, Y.; Fang, H.; Luo, W.; Xu, F.; Liu, L.; Wang, B.; Zhang, X.; Yang, D.; Hu, W. Generalized colloidal synthesis of high-quality, two-dimensional cesium lead halide perovskite nanosheets and their applications in photodetectors. *Nanoscale* **2016**, *8*, 13589–13596. [[CrossRef](#)]
69. Horvath, E.; Spina, M.; Szekrenyes, Z.; Kamaras, K.; Gaal, R.; Gachet, D.; Forro, L. Nanowires of methylammonium lead iodide ( $\text{CH}_3\text{NH}_3\text{PbI}_3$ ) prepared by low temperature solution-mediated crystallization. *Nano Lett.* **2014**, *14*, 6761–6766. [[CrossRef](#)] [[PubMed](#)]
70. Zhu, C.; Tang, Y.; Chen, F.; Manohari, A.G.; Zhu, Y.; Shi, Z.; Xu, C. Fabrication of self-assembly polycrystalline perovskite microwires and photodetectors. *J. Cryst. Growth* **2016**, *454*, 121–127. [[CrossRef](#)]
71. Xiao, R.; Hou, Y.; Fu, Y.; Peng, X.; Wang, Q.; Gonzalez, E.; Jin, S.; Yu, D. Photocurrent Mapping in Single-Crystal Methylammonium Lead Iodide Perovskite Nanostructures. *Nano Lett.* **2016**, *16*, 7710–7717. [[CrossRef](#)]
72. Spina, M.; Lehmann, M.; Nafradi, B.; Bernard, L.; Bonvin, E.; Gaal, R.; Magrez, A.; Forro, L.; Horvath, E. Microengineered  $\text{CH}_3\text{NH}_3\text{PbI}_3$  Nanowire/Graphene Phototransistor for Low-Intensity Light Detection at Room Temperature. *Small* **2015**, *11*, 4824–4828. [[CrossRef](#)]
73. Chen, Y.; Wu, X.; Chu, Y.; Zhou, J.; Zhou, B.; Huang, J. Hybrid Field-Effect Transistors and Photodetectors Based on Organic Semiconductor and  $\text{CsPbI}_3$  Perovskite Nanorods Bilayer Structure. *Nano-Micro Lett.* **2018**, *10*, 57. [[CrossRef](#)]
74. Meng, Y.; Lan, C.; Li, F.; Yip, S.; Wei, R.; Kang, X.; Bu, X.; Dong, R.; Zhang, H.; Ho, J.C. Direct Vapor-Liquid-Solid Synthesis of All-Inorganic Perovskite Nanowires for High-Performance Electronics and Optoelectronics. *ACS Nano* **2019**, *13*, 6060–6070. [[CrossRef](#)]
75. Yang, T.; Zheng, Y.; Du, Z.; Liu, W.; Yang, Z.; Gao, F.; Wang, L.; Chou, K.C.; Hou, X.; Yang, W. Superior Photodetectors Based on All-Inorganic Perovskite  $\text{CsPbI}_3$  Nanorods with Ultrafast Response and High Stability. *ACS Nano* **2018**, *12*, 1611–1617. [[CrossRef](#)] [[PubMed](#)]
76. Du, Z.; Fu, D.; Teng, J.; Wang, L.; Gao, F.; Yang, W.; Zhang, H.; Fang, X.  $\text{CsPbI}_3$  Nanotube Photodetectors with High Detectivity. *Small* **2019**, *15*, e1905253. [[CrossRef](#)]
77. Kwak, D.-H.; Lim, D.-H.; Ra, H.-S.; Ramasamy, P.; Lee, J.-S. High performance hybrid graphene- $\text{CsPbBr}_{3-x}\text{I}_x$  perovskite nanocrystal photodetector. *RSC Advances* **2016**, *6*, 65252–65256. [[CrossRef](#)]
78. Surendran, A.; Yu, X.; Begum, R.; Tao, Y.; Wang, Q.J.; Leong, W.L. All Inorganic Mixed Halide Perovskite Nanocrystal-Graphene Hybrid Photodetector: From Ultrahigh Gain to Photostability. *ACS Appl. Mater. Interfaces* **2019**, *11*, 27064–27072. [[CrossRef](#)] [[PubMed](#)]
79. Zou, C.; Xi, Y.; Huang, C.Y.; Keeler, E.G.; Feng, T.; Zhu, S.; Pozzo, L.D.; Lin, L.Y. A Highly Sensitive UV-vis-NIR All-Inorganic Perovskite Quantum Dot Phototransistor Based on a Layered Heterojunction. *Adv. Opt. Mater.* **2018**, *6*, 1800324. [[CrossRef](#)]
80. Dou, L.; Yang, Y.M.; You, J.; Hong, Z.; Chang, W.H.; Li, G.; Yang, Y. Solution-processed hybrid perovskite photodetectors with high detectivity. *Nat. Commun.* **2014**, *5*, 5404. [[CrossRef](#)] [[PubMed](#)]
81. Fang, Y.; Huang, J. Resolving Weak Light of Sub-picowatt per Square Centimeter by Hybrid Perovskite Photodetectors Enabled by Noise Reduction. *Adv. Mater.* **2015**, *27*, 2804–2810. [[CrossRef](#)]
82. Lin, Q.; Armin, A.; Lyons, D.M.; Burn, P.L.; Meredith, P. Low noise, IR-blind organohalide perovskite photodiodes for visible light detection and imaging. *Adv. Mater.* **2015**, *27*, 2060–2064. [[CrossRef](#)] [[PubMed](#)]
83. Sutherland, B.R.; Johnston, A.K.; Ip, A.H.; Xu, J.; Adinolfi, V.; Kanjanaboos, P.; Sargent, E.H. Sensitive, Fast, and Stable Perovskite Photodetectors Exploiting Interface Engineering. *ACS Photonics* **2015**, *2*, 1117–1123. [[CrossRef](#)]
84. Zhao, Y.; Li, C.; Shen, L. Recent advances on organic-inorganic hybrid perovskite photodetectors with fast response. *InfoMat* **2019**, *1*, 164–182. [[CrossRef](#)]
85. Konstantatos, G.; Sargent, E.H. Nanostructured materials for photon detection. *Nat. Nanotechnol.* **2010**, *5*, 391–400. [[CrossRef](#)]
86. Dong, R.; Fang, Y.; Chae, J.; Dai, J.; Xiao, Z.; Dong, Q.; Yuan, Y.; Centrone, A.; Zeng, X.C.; Huang, J. High-gain and low-driving-voltage photodetectors based on organolead triiodide perovskites. *Adv. Mater.* **2015**, *27*, 1912–1918. [[CrossRef](#)] [[PubMed](#)]